Elevated physical weathering exceeds chemical weathering of clays during the Paleocene-Eocene Thermal Maximum in the continental Bighorn Basin (Wyoming, USA)

Ji, Kaipeng; Wang, Chaowen; Hong, Hanlie; Yin, Ke; Zhao, Chenlei; Prins, Maarten; Lourens, Lucas J.; Gingerich, Philip D.; Abels, Hemmo A.; More Authors

DOI
10.1016/j.palaeo.2023.111445

Publication date
2023

Document Version
Final published version

Published in
Palaeogeography, Palaeoclimatology, Palaeoecology

Citation (APA)
Ji, K., Wang, C., Hong, H., Yin, K., Zhao, C., Prins, M., Lourens, L. J., Gingerich, P. D., Abels, H. A., & More Authors (2023). Elevated physical weathering exceeds chemical weathering of clays during the Paleocene-Eocene Thermal Maximum in the continental Bighorn Basin (Wyoming, USA). *Palaeogeography, Palaeoclimatology, Palaeoecology*, *615*, Article 111445. https://doi.org/10.1016/j.palaeo.2023.111445

Palaeogeography, Palaeoclimatology, Palaeoecology 615 (2023) 111445

Contents lists available at ScienceDirect

Palaeogeography, Palaeoclimatology, Palaeoecology

journal homepage: www.elsevier.com/locate/palaeo

Invited Research Article

Elevated physical weathering exceeds chemical weathering of clays during the Paleocene-Eocene Thermal Maximum in the continental Bighorn Basin (Wyoming, USA)

Kaipeng Ji [a], Chaowen Wang [b,c,*], Hanlie Hong [a], Ke Yin [a], Chenlei Zhao [a], Yanxiao Xu [a], Bowen Song [d], Maarten Prins [e], Lucas J. Lourens [f], Philip D. Gingerich [g], Hemmo A. Abels [c]

[a] School of Earth Sciences, China University of Geosciences, Lumo Road 388, Wuhan 430074, China
[b] Gemmological Institute, China University of Geosciences, Lumo Road 388, Wuhan 430074, China
[c] Department of Geosciences and Engineering, Delft University of Technology, Stevinweg 1, Delft 2628CN, the Netherlands
[d] Institute of Geological Survey, China University of Geosciences, Lumo Road 388, Wuhan 430074, China
[e] Faculty of Earth Sciences, Vrije Universiteit Amsterdam, De Boelelaan 1085, Amsterdam 1081 HV, the Netherlands
[f] Department of Earth Sciences, Utrecht University, Princetonlaan 8a, Utrecht 3584 CB, the Netherlands
[g] Department of Earth and Environmental Sciences and Museum of Paleontology, University of Michigan, Varsity Drive 3600, Ann Arbor, MI 48108-2228, USA

ARTICLE INFO

Editor: A Dickson

Keywords:
Paleocene-Eocene Thermal Maximum
Polecat Bench
Smectite
Paleoclimatology
Continental weathering

ABSTRACT

The Paleocene-Eocene Thermal Maximum (PETM) global warming event at ~56 million years before present changed catchment weathering and erosion. Increased chemical weathering of silicate minerals is thought to be an important process removing CO_2 from the atmosphere. However, changes in clay mineralogy can often be explained by enhanced erosion of catchment laterites during the event. Here, we investigate chemical and physical weathering and erosive flux changes through the PETM interval in the Bighorn Basin, Wyoming, a Laramide foreland basin, in a proximal continental-interior alluvial setting. These show an increase of detrital smectite with a lag time of 20-kyr after the main onset the PETM. The smectite increase continued for at least 50-kyr after the event. In-situ, post-depositional pedogenic clay mineral formation is similar between pre-PETM and PETM soil profiles, despite large macroscopic differences between soils that formed before and during the event. Drier, hotter summers during the PETM probably caused decreased vegetation cover that, in concert with more frequent and heavier rainstorms, intensified the erosion of smectite-rich Cretaceous bentonites on the margins of the catchment, which exceeded changes in chemical weathering within the catchment. The lagged response in reaching full PETM clay mineral values can be explained by the time required for upstream sediment to reach the catchment basin floodplain. The prolonged nature of smectite enhancement after the PETM event may again relate to signal propagation times that are now even longer due to lower fluvial recycling rates. Our results indicate that chemical weathering changes were probably superceded by enhanced physical weathering and clay-mineral transport from basin margins at this continental-interior study site.

1. Introduction

In a series of transient hyperthermal events in the Cenozoic Era, the Paleocene-Eocene Thermal Maximum (PETM; ca. 56 Ma) and Eocene Thermal Maximum 2 (ETM2; ca. 53.5 Ma) have been considered to be the prominent warming events (Kennett and Stott, 1991; Zachos et al., 2001; Lourens et al., 2005; Zeebe et al., 2016), The PETM was documented both in marine and terrestrial archives with distinct carbon isotope excursion (CIE) by −3‰ and − 7‰ (Kennett and Stott, 1991; Koch et al., 1992; McInerney and Wing, 2011), respectively, and with the total duration spanning ~94 kyr to ~231 kyr (Giusberti et al., 2007; Röhl et al., 2007; Murphy et al., 2010; Zeebe and Lourens, 2019; Van der Meulen et al., 2020). During the PETM, an estimated 2000–12,000 Gt ^{13}C-depleted carbon was rapidly pumped into the ocean-atmosphere system (Giusberti et al., 2007; McInerney and Wing, 2011; Gutjahr et al., 2017). As a consequence, the global mean temperature dramatically increased by ~5 to 8 °C, accompanied by mass extinction of marine organisms, ocean acidification, turnover of flora and fauna, and

* Corresponding author at: Gemmological Institute, China University of Geosciences, Lumo Road 388, Wuhan 430074, China.
E-mail address: c.w.wang@cug.edu.cn (C. Wang).

https://doi.org/10.1016/j.palaeo.2023.111445
Received 2 May 2022; Received in revised form 2 February 2023; Accepted 8 February 2023
Available online 13 February 2023

dwarfing of mammal taxa (Kennett and Stott, 1991; Clyde and Gingerich, 1998; Gingerich, 2003; Wing et al., 2005; Zachos et al., 2005; Bralower et al., 2018; Inglis et al., 2020). The PETM, as a global warming caused by greenhouse gases, parallels ongoing anthropogenic warming. Hence, despite occurring at times of different climate and geographic backgrounds, the PETM is generally considered the best geological analogue to understand climate change and earth system response to rapid, large emissions of CO_2.

The mechanism of carbon removal during the PETM is the key to better understand how the earth recovered from the high CO_2 concentration in the atmosphere-ocean system. Chemical weathering of silicate minerals was thought to be one of the vital negative feedback mechanisms to sequester atmospheric CO_2, apart from the regrowth of organic carbon stocks (Bowen and Zachos, 2010), enhancement of primary production (Ma et al., 2014), and carbonate dissolution and subsequent limestone deposition (Penman et al., 2016). Clay minerals as chemical weathering products of silicates have widely been used as an index for global warming and enhanced chemical weathering. In some marine and coastal sediments, the increased proportion of kaolinites and indices of clay assemblage coeval with the CIE have been interpreted as intensified chemical weathering, such as sedimentary records from the Antarctica (Robert and Kennett, 1994), the North Atlantic (Gibson et al., 1993, 2000; Zachos et al., 2006), the Tethys (Bolle and Adatte, 2001), and the Arctic Ocean (Dypvik et al., 2011). However, this point of view has been challenged as evidence points to simultaneous increases of terrestrial sediment input coeval with the increase of kaolinite during the PETM (Sluijs et al., 2008; Zacke et al., 2009; Soliman et al., 2011). Alternatively, these findings have been attributed to intensified physical weathering (John et al., 2012; McInerney and Wing, 2011), as observed higher seasonal precipitation and greater surface runoff increase supplies of terrigenous sediments from adjacent landmasses during the PETM (Soliman et al., 2011; Handley et al., 2012). Other weathering-sensitive proxies such as Li, Os, and Si isotope records, have been documented for marine and coastal sediments. The Os and Li isotope records documented an enhanced weathering and erosion (Wieczorek et al., 2013; Pogge von Strandmann et al., 2021), while the Si isotope record revealed a low intensity of continental chemical alteration (Rad et al., 2009). Identifying chemical weathering over physical weathering plays a vital role on understanding the mechanisms the carbon removal, as the chemical weathering is considered to increase the uptake of carbon from the atmosphere, while the physical weathering controls the organic carbon burial. Such evidence of continental weathering is still lacking, thus impeding the evaluation of the efficiency of carbon removal by chemical weathering.

The Bighorn Basin is a remote intermontane basin filled by alluvial sediments spanning the Paleocene to Eocene (Kraus et al., 2015; Abels et al., 2016) and providing a good opportunity to study the effect of hyperthermal on continental weathering during the PETM. The PETM in the series is depicted by strong changes in paleosol development in PETM outcrops throughout the Bighorn Basin (Kraus et al., 2015). PETM paleosoils are thicker, show more pedogenic features, are more often red and purple coloured, and contain more pedogenic carbonate. The PETM is very well constrained in the floodplain stratigraphy by carbon isotope records of pedogenic carbonate (Koch et al., 1992; Bowen et al., 2001; Van der Meulen et al., 2020). In this paper, we report on new high-resolution clay mineralogical and grain-size records from the Polecat Bench section in the northern Bighorn Basin spanning the Paleocene-Eocene Thermal Maximum. We evaluate the clay mineral changes in view of grain-size sorting, in situ soil formation, and detrital influx in these floodplain deposits based on the developed methodology of Wang et al. (2017). The analysis offers the unique opportunity to ascribe changes to physical weathering and/or chemical weathering during the PETM and place these findings in a global paleoenvironmental and paleoclimatic perspective.

2. Geological setting

The Bighorn Basin, in northern Wyoming, was a foreland basin that has experienced a series of tectonic activities in Mesozoic to early Cenozoic times (Fanshawe, 1971). The basin was the part of the Cordilleran foreland Basin during the Late Jurassic time, which was subsequently partitioned as structural basin because of the Laramide orogeny during the Late Cretaceous–early Eocene (Fan and Carrapa, 2014). The increased rock uplift rates during the late Paleocene–early Eocene enhanced the intermontane basin subsidence in the region, such as in the Bighorn Basin (Omar et al., 1994; Fan and Carrapa, 2014).

The current Bighorn Basin is bounded by the Bighorn Mountains in the east, Owl Creek Mountains in the south, and the Beartooth and Absaroka Mountains in the west, respectively (Fig. 1). In response to the uplift, Cenozoic detritus grade from fan conglomerates at the basin margins into channel and floodplain sandstones and mudstones in the basin center. In the basin axis, the paleocurrent directions point northward (Neasham and Vondra, 1972; Welch et al., 2022; Wang et al., 2022a). Provenance studies have demonstrated that the source rocks were granites, granite-gneiss, sandstones, shales, red siltstones, carbonates (dolomites and limestones) and evaporates (Neasham and Vondra, 1972). These rock assemblages are similar to the exposed rocks proximal to the Beartooth Mountains (Fig. 1, Thomas, 1965; Omar et al., 1994; Welch et al., 2022).

The Bighorn Basin captures one of the most complete terrestrial stratigraphic records across the Paleocene-Eocene boundary straddling the transition from the grey-bedded Fort Union Formation to red-bedded Willwood Formation (Kraus and Gwinn, 1997). The Fort Union Formation is widely distributed in the Bighorn Basin and mainly comprises fluvial sandstones, drab mudstones, grey and green-grey paleosols, carbonates, and occasional lignites (e.g., Kraus, 1998). The Willwood Formation is dominated by fluvial deposits characterized by red, purple, and yellow-brown paleosols, and heterolithic sandy deposits with weakly pedogenic development, and mudstones with strong pedogenic development, and channel and sheet sandstones (Kraus and Gwinn, 1997).

The Polecat Bench (PCB) section crops out below a Pleistocene river terrace in the northern of the Bighorn basin. It is the first location that recorded the carbon isotope excursion (CIE) of the Paleocene-Eocene Thermal Maximum on land (Koch et al., 1992). The measured portion of the PCB section (GPS: 43°15′30.4”N, 108°43′35.2”W) is ~140 m thick and is composed of the uppermost Fort Union Formation and the lower Willwood Formation across the Paleocene-Eocene boundary (Fig. 1). Several studies have documented the PETM in the section using bulk sediment organic and pedogenic carbonate isotopes (Magioncalda et al., 2004; Bowen et al., 2001). The section studied here is described in detail by Van der Meulen et al. (2020) who produced a high-resolution carbon isotope stratigraphy using pedogenic carbonate nodules. A pronounced $\delta^{13}C$ shift from −10 ‰ to −14 ‰ at the ~65 m stratigraphic level that marks the main PETM onset. In the main body, $\delta^{13}C$ remain light while gradually increasing until at the ~100 m stratigraphic level where $\delta^{13}C$ values rapidly increased, marking the start of the PETM recovery phase. Between the step and the 120 m lever the full recovery occurs (Van der Meulen et al., 2020).

3. Sampling and methods

A series of trenches were excavated at a depth of 25–100 cm and a width of 50–100 cm along the terrain to yield a continuous floodplain section and exclude samples influenced by present-day weathering. Trenches were located in the field to avoid major channel sand bodies and compile a composite where the terrain allows access and outcrop. Samples were collected from the PCB section at 0.25 m spacing measured using a Jacob's Staff. Field descriptions were in accordance with the study of Abels et al. (2013) and follow Van der Meulen et al. (2020).

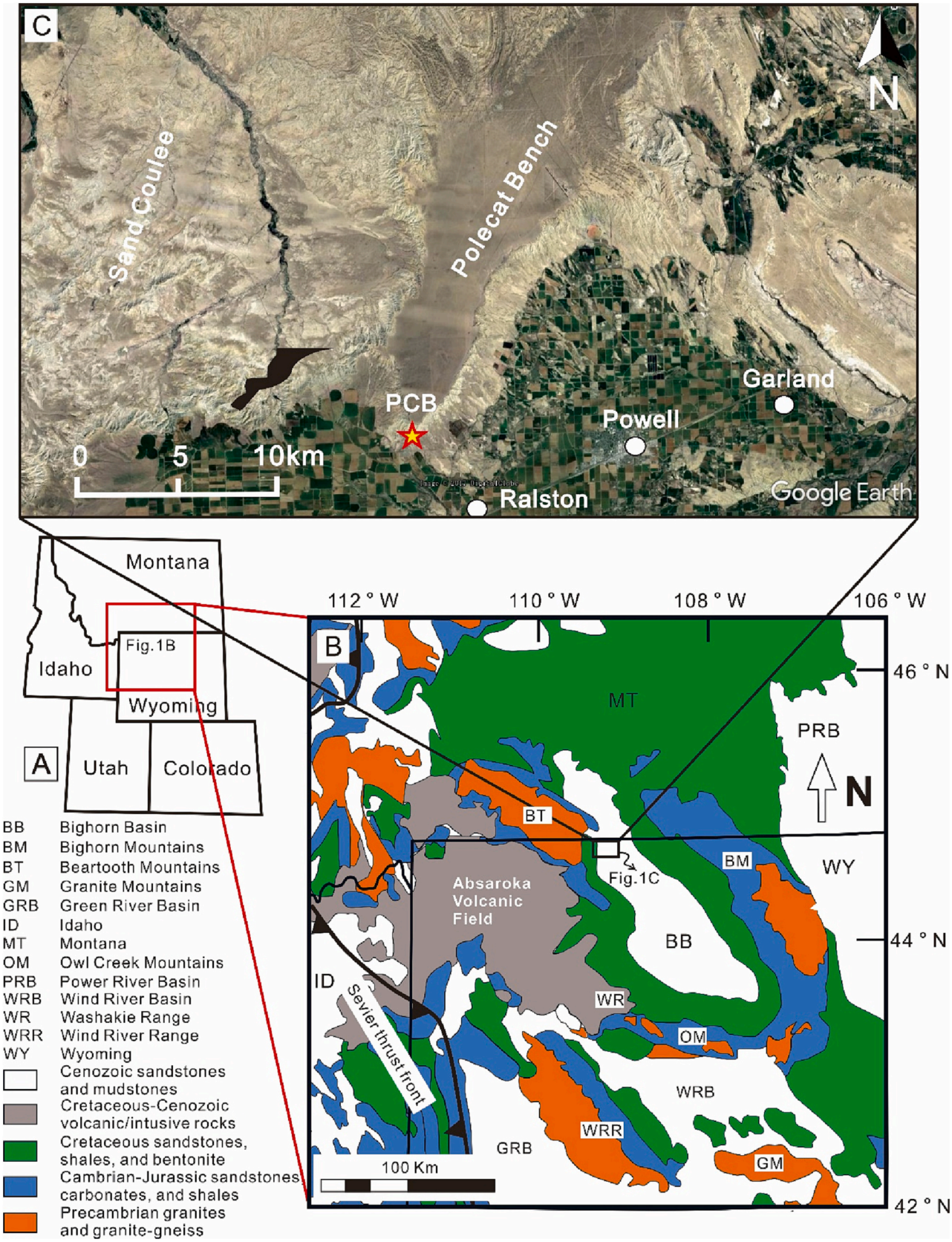

Fig. 1. (A) Location of the Bighorn Basin in northern Wyoming; (B) Simplified geological map of the Bighorn Basin and location of the Palecat Bench area, modified from Fan and Carrapa (2014); (C) Satellite image map showing the location of Palecat Bench (PCB) section in the Bighorn Basin from the Google Earth.

3.1. Grain size analysis

A total of 160 samples were selected with an interval of 1 m to perform grain size in the sedimentological laboratory, Vrije Universiteit (VU), Amsterdam, Netherlands. Five grams of sample material was used for analyses before carbonate and organic matter were removed by 10 mL 30% H_2O_2 and 10 mL 10% HCl respectively, prior to the analysis. All samples were treated with $Na_4P_2O_7{\cdot}10H_2O$ and an ultrasonic transducer for 5 min to further disperse grains. Grain size statistics were gathered using a Sympatec HELOS/KR laser-diffraction particle size measurer with advanced wet disperser QUIXEL. The results of grain size distributions were divided into 57 sections, ranging from 0.1 to 2000 μm. Information of median (D_{50}) and mean grain size, standard deviation, skewness, kurtosis, and percentages of clay, silt, and sand were calculated automatically. All particles <8 μm were determined to be clays. The silts domain falls within the 8–63 μm interval, and sands fall within the 63–2000 μm interval. In order to reflect the competence and information of the hydrodynamic condition, median grain size (D_{50}) was applied to represent the distribution of each sample (Knighton, 1999).

3.2. XRD analysis

A subset of 166 whole-rock paleosol samples was manually ground to powder (finer than 0.074 mm) using an agate mortar and pestle. Preparation of oriented clay samples and ethylene glycol (EG) saturated clay samples followed the method of Jackson (1975) and Zhao et al. (2021).

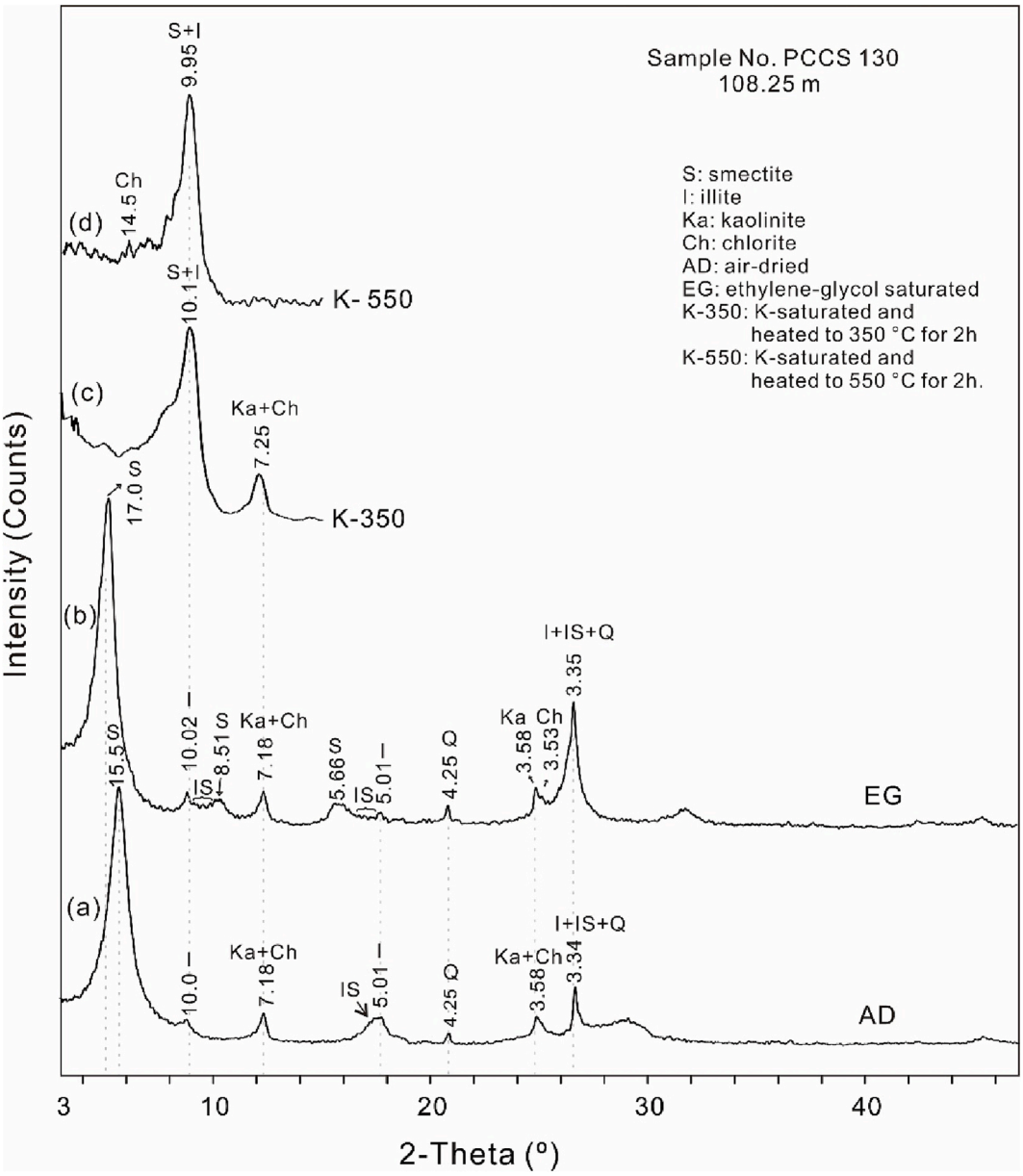

Fig. 2. Paralleled XRD patterns of clay minerals in sample PCCS 130. The patterns a, b, c, and d, denote the XRD curves after AD, EG, K-350, and K-550 treatments. The unit of valued peak position is angstrom (Å). Notably, the peak swelled from 15.5 Å (a) to 17 Å (b) after EG treatment, and collapsed to 10 Å after K-350 °C and K-550 °C treatments, indicating the present of smectite in the sample. The peak positions stayed no shift in both AD (a) and EG (b) patterns at ~10 Å and ~ 5 Å, indicating the existence of illite. The emergence of the broad peaks in EG (b) pattern between the d_{001} and d_{002} reflections of illite (10 Å) and smectite (8.51 Å) as well as the d_{002} and d_{003} reflections of illite (5 Å) and smectite (5.66 Å), respectively, compared with AD (a) pattern, reflected the existence of irregular mixed-layered illite-smectite. The peaks at ~7.2 Å and 3.58 Å stayed the same in AD (a) and EG (b) patterns, and the ~7.2 Å peak stayed at K-350 (c) patterns and collapsed after heating at 550 °C, indicating the existence of Kaolinite. Small shoulder at the right of the 3.58 Å peak in EG pattern and enhanced 14.5 Å peak after K-550 °C treatments reveal the presence of chlorite, even though it is less obvious indicating the less amount of chlorite.

During the procedure, about 150 mLbuffer solution ($CH_3COONa{\cdot}3H_2O$ and CH_3COOH) and 15 mL 30% H_2O_2 were used to remove carbonates and organic matter from the whole powder samples, respectively. <2 μm fractions were disengaged from the sample using sequential centrifugation with multiple times ultrasonic treatments dispersing clay aggregation. Next, Na-bearing (NaCl) reagents were added to flocculate clays overnight for further homogenization. To prevent peak overlaps of Na-bearing from Ca-bearing clays between mixed-layer illite-smectite (I/S) and mixed-layer illite-vermiculite (I/V), as well as between vermiculite and Na-smectite in the XRD, the Ca-form clay species were obtained by washing samples three times with 1 mol/L $CaCl_2$, followed by removal of Ca^{2+} and Cl^{-}via dialysis using a semipermeable membrane. We used four paralleled clay slides to identify clay minerals (Fig. 2): (1) air-dried (AD) oriented clay slides, which was made by clay slurries settling onto glass slides. (2) Ethylene-glycol (EG) saturation slides were obtained by using AD slides treated with saturated ethylene glycol vapor in a desiccator at 65 °C for 4 h, (3) K-350 slide was prepared by using clay slurry, which was then saturated with 1 M KCl and heated at 350 °C for 2 h, and (4) K-550 slide was obtained by heating K-350 °C slide for 2 h.

The clay mineral composition was measured by X-ray diffraction (XRD) using a Dandong TongDa TDX-3500 X'pert PRO diffractometer with Ni filtered Cu Kα radiation, at State Key Laboratory of Biogeology and Environmental geology. Under 45 kV and 30 mA working conditions, XRD patterns of paralleled clay slides were recorded with a step size of 0.02° 2θ/s and speed of 2 s/step, ranging from 3 to 47° 2θ for AD and EG slides and 3 to 15° 2θ for K-heated slides, respectively.

Semi-quantification of clay minerals was achieved by using the software Newmod II based on primarily identified clay mineral assemblages (Reynolds and Reynolds, 2012). Before best-fit can be obtained, the crystal-chemical curves for each clay mineral were adjusted. The detailed process for setting of parameters for smectites, illite, and I/S can refer to Zhao et al. (2021). Peak of kaolinites at ~7.2 Å was fitted by two types of kaolinites with "smaller and larger" mean crystallite thickness at 7.30 and 7.16 Å, respectively. When a close match on EG pattern was achieved between experimental and simulated XRD patterns, a best-fit curve was generated and the proportions of each clay mineral were obtained (Fig. 3).

3.3. Scanning electron microscopic (SEM)

Five samples of well-developed paleosols and non-pedogenically modified mudstones from the three time intervals (the Pre-PETM, PETM, and Post-PETM) were subjected to SEM analyses. These samples are PCTP-32 (49.625 m), PCCS-30 (83.125 m), PCCS-66 (92.125 m), PCCS-130 (108.125 m), and PCCS-150 (113.125 m). Observations of sediment and mineral morphologies and analyses of mineral element composition were carried out on the equipment HITACHI FEG-SEM,

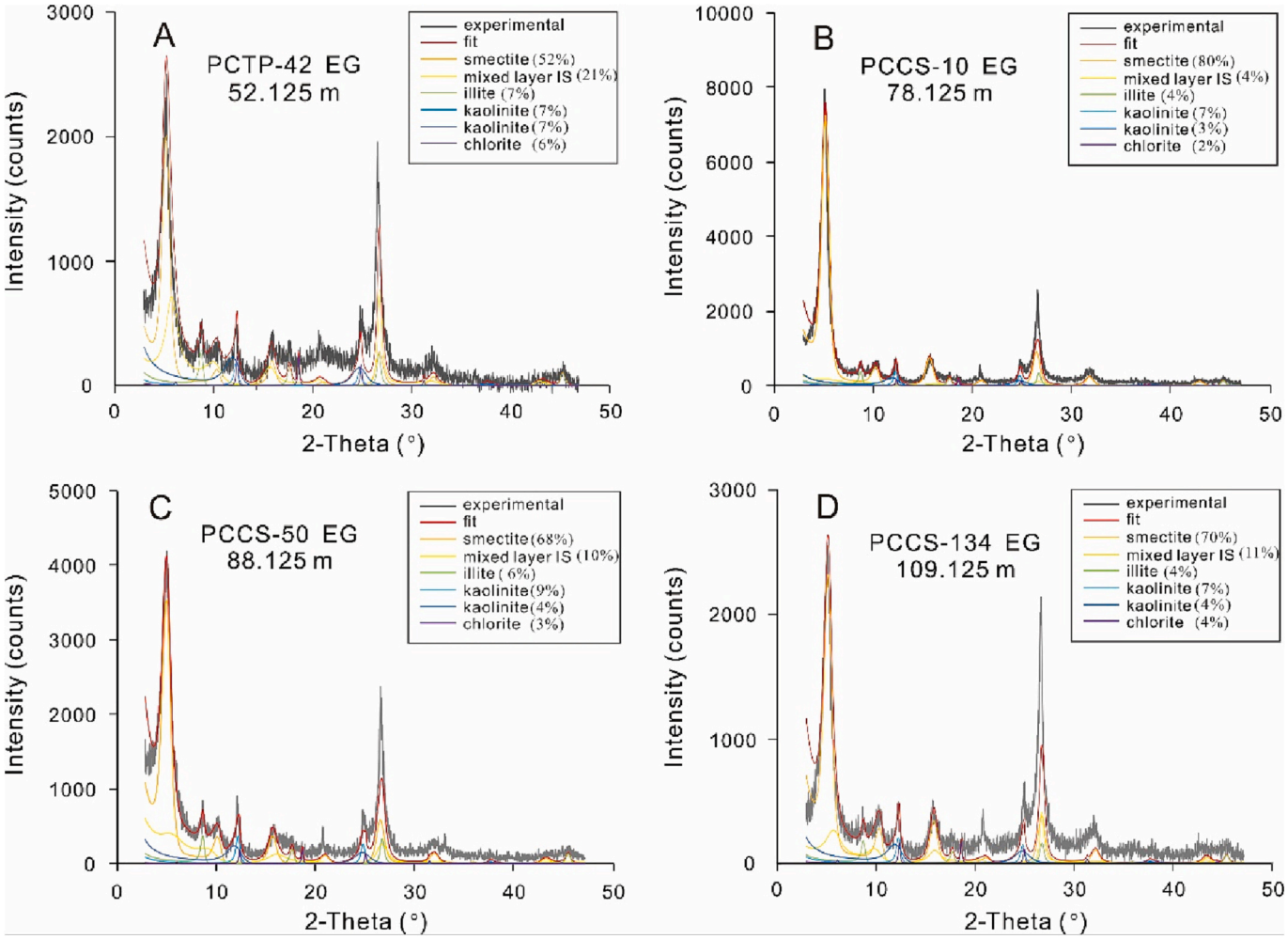

Fig. 3. Examples of fitted XRD profiles with different grain-size and stratigraphic levels using program Newmod II based on the EG state. (A) PCTP-42 from the pre-PETM with median grain size between 4 μm and 16 μm. (B) PCCS-10 from the PETM with median grain size larger than 16 μm. (C) PCCS-50 from the PETM with median grain size <4 μm. (D) PCCS-134 m from the post-PETM with median grain size larger than16 μm. Both kaolinites with larger and smaller mean crystallite thickness were used here to fit profiles well.

equipped with an energy dispersive spectrometer (EDS) at China University of Geoscience, Wuhan. Freshly broken samples were applied and preliminary Au-coated before measurements. The EDS used to identify the elementary composition of minerals was operated at 10–20 kV accelerating voltage and 3–5 nA beam current.

3.4. Statistical methodology for clay mineralogical data

In the Bighorn Basin, the proportions of clay minerals could be affected by the lithology and the grain size of river floodplain sediments deposited during and outside the PETM interval, which could be related to overbank and avulsion sedimentation, pedogenesis and PETM event (Kraus and Riggins, 2007; Abels et al., 2012, 2013; Foreman, 2014; Kraus et al., 2015; Abels et al., 2016; Wang et al., 2017). To constrain factors above, we tested the clay mineralogical distribution to evaluate the proportions of clay minerals for their dependence on different grain-size classes (median value <8 μm and > 8 μm) of samples. Differentiation was made between samples of sediments that show no or weak and those that show strong pedogenesis, and samples from preceding, inside, and post-dating the PETM interval. Grain-sizes were binned with an 8 μm boundary because clay fractions have a grain size up to 8 μm as defined by the Laser Particle Sizer (Konert and Vandenberghe, 1997). The influence of pedogenesis was analyzed using the soil development index (SDI) as calculated by Van der Meulen et al. (2020). Binning of samples based on SDI was done in accordance with the method of Wang et al. (2017) who distinguish limited to intermediate paleosol development with a SDI value <1.0 and intense pedogenesis with a SDI values >1.0.

An analysis of variance (ANOVA) was performed by MS Excel 2010 to evaluate the proportional similarities /differences of clay minerals, with statistical significance defined as $p < 0.05$. If $p < 0.05$, the similarities/differences were accepted at a 95% confidence level.

4. Result

4.1. Floodplain grain-size distributions

The grain-size distribution of all floodplain samples of the PCB section ranges between 2 μm and 170 μm, containing 51% clays, 38% silts, and 11% sands on average (Table 1). The proportions of these grain sizes reveal no statistical relevant variation among the Pre-PETM, PETM, and Post-PETM stratigraphic intervals. The median grain size along the PCB section exhibits no statistical significance, while displaying a slight decrease during the PETM compared with Pre-PETM and Post-PETM intervals (Table 1, Supplement fig. 1). Note that these samples were sampled in a vertical stratigraphic composite through floodplain strata and major sand bodies were excluded. The lack of grain-size changes through the PETM event is thus valid for the floodplain sediments in this part of the northern Bighorn basin.

Table 1
Grain size distribution of the PCB section showing no significant change of grain size across the PETM.

Grain-size classes	Clays (μm)	Silts (μm)	Sands (μm)	Median (D_{50})
	< 8	8–63	63–2000	μm
Average	**50.73**	**37.8**	**11.5**	**14.9**
S. D.	19.9	12.3	14.1	15.5
Pre-PETM	**50.6**	**37.4**	**12.0**	**15.2**
S. D.	20.9	13.1	15.3	17.5
PETM	**51.2**	**38.2**	**10.6**	**13.0**
S. D.	16.3	9.1	13.5	12.2
Post-PETM	**51.4**	**38.0**	**10.6**	**15.9**
S. D.	21.4	13.2	11.5	12.0

4.2. Floodplain sediment microtexture

Scanning Electron Microsopy (SEM) reveals that the floodplain sediments of the Polecat Bench section display a matrix-supported, loose texture. Mineral particles in sediments mainly occur as clastics and their morphologies vary from subangular to subrounded (Fig. 4A). Most clay minerals cover the surface of detrital particles or fill in the gaps between these particles. Clay minerals exist as thin sheets with size ranges from submicron to tens of microns. The basal (001) planes of clay particles have smooth surfaces, and display random arrangements of directions (Fig. 4B). Most smectites exhibit sheet-like morphology with irregular and curly edges (Fig. 4C). The edges of the dissolved clay particles are embayed and streamlined. Large aggregations of mica are rare and show subangular shapes, diameters of up to 30 μm, and undissolved surfaces (Fig. 4D).

There are two forms of smectites in soil B horizons observed under SEM. The first one is most common and shows flake-shaped smectite with grain sizes of 1 to 10 μm (Fig. 4C, D, and E). The second is uncommon and are smectite aggregations of <2 μm showing honeycomb structures (Fig. 4F).

4.3. Floodplain clay mineral identification and composition at Polecat Bench

Identification of clay minerals was mainly carried out based on the characteristic reflections on combined XRD diagrams of paralleled clay slides (Moore and Reynolds, 1997). In AD XRD pattern, d_{001} reflection peaks of smectite, illite, and kaolinite are identified at the peaks of 15.5 Å, ~10 Å, ~7.2 Å, respectively (Fig. 2). The d_{001} reflection peak of smectite shifted to 17 Å after EG treatment accompanied by obvious occurrence of broad peaks of d_{002} and d_{003} reflections at 8.51 Å and 5.66 Å, respectively, while the illite and kaolinite displayed no shift. The chlorite can be identified based on emerged peak at 3.53 Å for d_{003} reflection peak after EG treatment. Under the K-350 °C treatment, the d_{001} reflection peak of smectite collapses to 10 Å, while the peaks of other clay minerals remain unchange. The K-550 °C treatment further caused the d_{001} reflection peak at ~7.2 Å of kaolinite and chlorite disappeared (Fig. 2). Irregular I/S was measured at bumps between d_{001} and d_{002} reflections of illite (10 Å) and smectite (~8.51 Å) as well as d_{002} and d_{003} reflections of illite (5 Å) and smectite (~5.66 Å), respectively (Fig. 2).

The clay mineral assemblage of the PCB section dominantly consists of smectite, with minor contributions of interlayered illite/smectite, and kaolinite (Supplement Table 1). Abundance of smectite ranges from 37 to 90% with an average of 66% (Fig. 5). I/S and kaolinite have contents ranging from 1 to 28% and on average 12% and 4–45% and on average 13%, respectively. Illite and chlorite occur as minor components with contents of 2–13% and on average 6%) and 1–7% and on average 3%, respectively.

4.4. Floodplain clay mineralogy dependence on grain size

We divided the grain sizes into two grain-size classes by median grain-size to facilitate the discussion of the relationship between particle size and clay mineral content. In order to minimize the impacts of pedogenesis and hyperthermal event of the PETM, samples from outside the PETM are analyzed. The proportion of smectite increases by 4.0% on average ($p = 0.0372$) from <8 μm to >8 μm median grain size samples with limited soil development (SDI < 1) from outside the PETM (Fig. 6a). Decrease of smectite by 3.7% ($p = 0.4304$) are observed from samples of these two grain size classes with good soil development (SDI >1) from outside the PETM (Fig. 6b). These increases of smectite both in SDI < 1 and SDI >1 are significant in the ANOVA test, even though the standard deviations of the smectite proportions display a large range. Kaolinite shows a slight change with an increase of median grain size, while illite and I/S show a decreasing trend with increasing grain size,

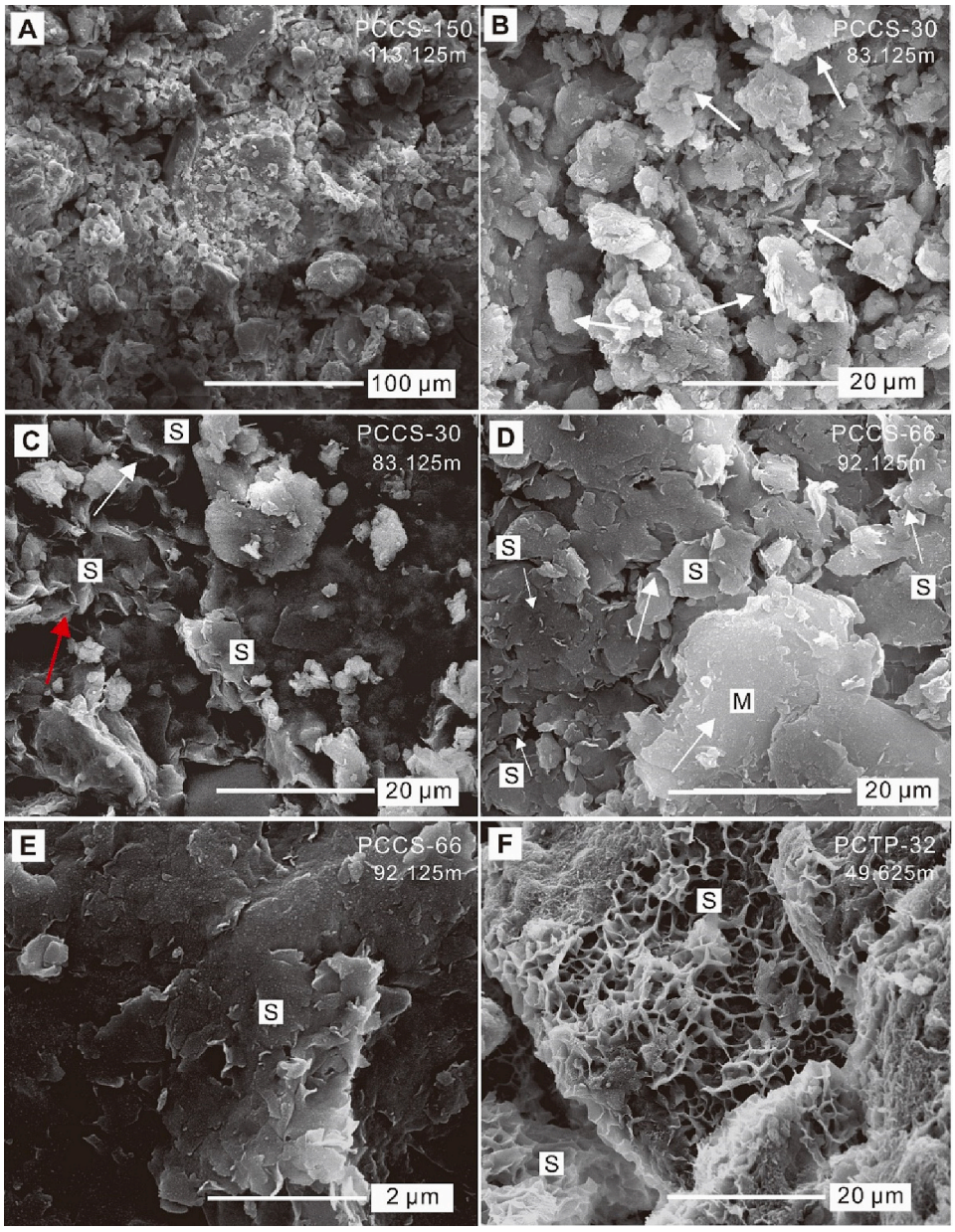

Fig. 4. SEM observation of clay minerals and non-clay minerals in samples of the Polecat Bench section. (A) Matrix-supported sediments with detrital minerals showing subangular to subcircular shapes. Clay debris occurring in the sediments by two forms: covering the surface of detrital particles and filling the voids between detrital particles. (B) Detrital clay minerals appear as thin platy morphology, random arrangement of direction (white arrow). (C) Detrital smectite (S) exhibit sheet-like morphology (white arrow) and irregular 001 plane with curved edges (red arrow). (D) Detrital mica (M) particle showing dissolved and embayed edge, and inherited smectite (S) occurring as thin flakes with curved edges. (E) Aggregated smectite (S) composing of small flakes with irregular 001 plane and curved edges. (F) Authigenic smectite (S) showing honeycomb shapes. (For interpretation of the references to colour in this figure legend, the reader is referred to the web version of this article.)

which is the opposite of smectite. Chlorite shows no change (Fig. 6a).

4.5. Soil development impact on clay mineralogy

Sediments with the same median grain size sediments of <8 μm, which should be less likely affected by grain-size sorting, are analyzed for the impact of in situ pedogenesis after deposition, both during the PETM and outside the PETM. All clay minerals in sediments from outside the PETM and during the PETM do not show significant average differences both in samples that show high and low post-depositional pedogenesis (Fig. 6c and d). In clay minerals, the smectite is similar, either decreased by 0.6% ($p = 0.7769$) or increased by 0.4% ($p = 0.9108$) on average from samples outside the PETM and during the PETM, respectively, from SDI < 1 to SDI > 1 because of pedogenesis (Fig. 6c and d).

4.6. Impact of the PETM on floodplain clay mineralogy

A 17-point moving average and the average values for each identified precession-cycle are calculated to analyze the long-term trends of clay mineralogy in relation to the PETM event (Fig. 5, supplementary data table). Kaolinite and illite display slightly decreasing trends into the PETM stratigraphic interval. Smectite displays a significant increasing trend from precession cycle - 4 onwards through the whole section. Smectite values more rapidly increase into the PETM body from cycle 1 to cycle 2 to stay approximately similar for the remainder of the section post-dating PETM (Fig. 5). The contents of I/S exhibits a mirrored trend of smectite. Notably, also I/S content changes from cycle 1 to cycle 2 within the main body of the PETM lagging the onset of the PETM by one precession cycle in the age model of Van der Meulen et al., 2020. The chlorite content shows an opposite trend with smectite, although the proportion of chlorite is small and its quantitative reconstruction therefore remains uncertain.

In the PETM, smectites intensively increased on average in total by 11.5% ($p = 0.0000$) in the floodplain sediments deposited during the PETM compared to Pre-PETM (Fig. 6e). This increase of smectites was significant and both observed, on average, 12.3% ($p = 0.0000$, Supplement Fig. 1a, b) for the samples displaying low pedogenesis (SDI < 1)

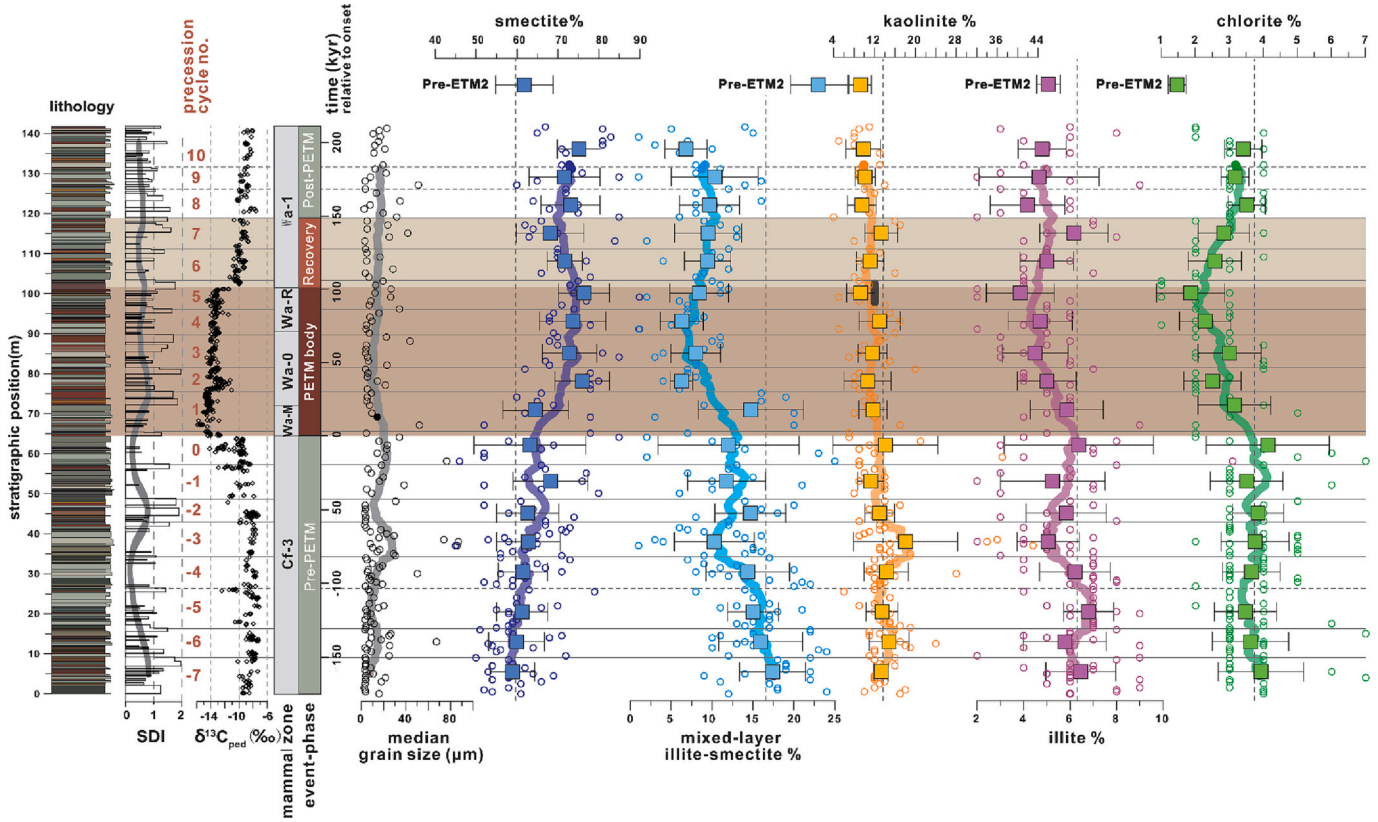

Fig. 5. Integrated multiple indices along with the sedimentological lithological log in the PCB section. Indices of soil development index (SDI), paleosol carbonate $\delta^{13}C$, and the timescale to relative onset of the PETM were referred to Van der Meulen et al. (2020). The American land-mammal zones were cited from Gingerich (2003). The median grain size showing slight decrease on average during the PETM with high uncertainty (data are shown in Table 1), compared to pre- and post-PETM. A curve of 130-point moving average of SDI values was in grey with an interval of 10 cm, showing no significant pedogenic differences among pre-PETM, PETM, and post-PETM. For each clay mineral index, 17-point and precession paced 7–8 m moving averages were applied with 7–8-m average standard deviation error bars to model the general tendency of clay mineral shifts at different stages. A significant lagged increase of smectite was observed at the onset of the PETM, with distinct decrease of mixed-layer illite-smectite and chlorite. The dark grey-shaded area highlights the body of the PETM and the grey-shaded area highlights the recovery of the PETM. Grey dashed lines and full lines are boundaries of precession cycles, which were marked by red numbers according to Van der Meulen et al. (2020). Boxes in different clay mineral curves stand for the averages of each clay mineral of precession cycles, respectively. Data of clay mineral proportions of Pre-ETM2 are from Wang et al. (2017). (For interpretation of the references to colour in this figure legend, the reader is referred to the web version of this article.)

and 9.7% ($p = 0.0005$, Supplement Fig. 1c, d) in samples displaying intense pedogenesis (SDI > 1). The smectites decreased by 0.4% ($p = 0.0794$) during the post-PETM compared to PETM (Fig. 6f). Even though the smectite have no significant difference between the PETM and post-PETM in the PCB section, the proportions of smectites after the post-PETM go back to pre-PETM level during the pre-ETM2, 1.8 Ma years later than the PETM (Fig. 6e, f). These data have been gathered in the Deer Creek area of the northern Bighorn Basin by Wang et al. (2017).

I/S and kaolinite were lower in the PETM interval. Proportions of I/S decreased by 5.7% (p = 0.0000) and 0.5% ($p = 0.7014$) in the PETM compared to those during the Pre-PETM and the Post-PETM. For kaolinite, its amount decreased by 3.4% ($p = 0.0018$) and increased by 0.4% ($p = 0.5363$) in the PETM compared to those during the Pre-PETM and the Post-PETM. The changes of illite and chlorite among Pre-PETM, PETM, and the Post-PETM, are slight and insignificant.

5. Discussion

5.1. Floodplain clay mineralogy in the Bighorn Basin

Types and proportions of clay minerals in avulsion- and the overbank-deposits could be affected by complex factors, such as provenance, hydraulic sorting, weathering changes, and diagenesis (Wang et al., 2016, 2017). The provenances of the Paleogene-Eocene sediments in Bighorn Basin were documented to be proximal at basin margins with differences in fan conglomerate while homogeneous in the distal northern Bighorn Basin. Multiple lines of evidence from field observations, petrological analysis, and detrital age distributions have documented the differences of provenance in complex associations of conglomerate at the Beartooth Mountain and the Absaroka Mountain fronts (Malone et al., 2017; Neasham and Vondra, 1972). The floodplain is characterized by a fairly stable and uniform mineralogical composition of the sediments (Wang et al., 2017; Welch et al., 2022), despite the geologic heterogeneity of the catchments and the significant grain-size sorting (Fig. 6a. b).

Detrital zircon geochronology of samples from Fort Union and Willwood Formations at the base and southwest end of Polecat Bench reveal similar age spectra. That indicates no change of provenances in the study site of PCB from the Paleogene to Eocene (May et al., 2013). This interpretation agrees with that made by Welch et al. (2022) using the provenance analysis of sandstones across the basin spanning the Paleogene to early Eocene period. Indeed, an increase of rock uplift rates in the Bighorn and Beartooth Mountains during the late Paleocene–early Eocene took place related to the rollback and associated retreating delamination of the Farallon oceanic slab (Fan and Carrapa, 2014). The subsidence of the Bighorn Basin in response to the rock uplift could have generated an adjustment of river gradients, leading to change of sediment transportation, rather than a change of provenance, as evidenced by modulated thickness, laterally-extensive size, and grain-size of sandstones (Foreman et al., 2012; Foreman, 2014; Welch et al., 2022)

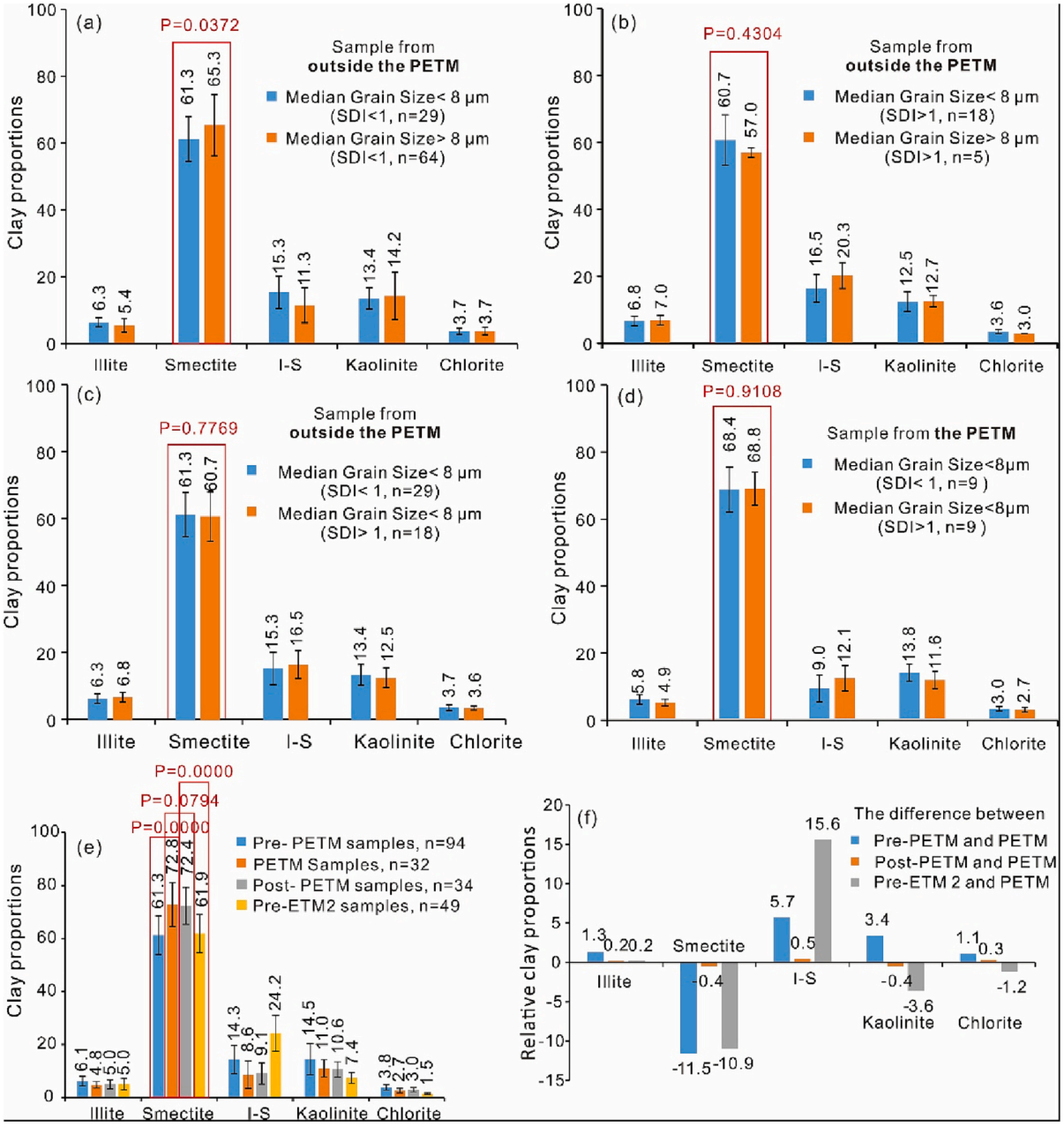

Fig. 6. Average clay mineral distribution (<2 μm) in different grain-size classes and soil development index (SDI) from samples during and outside the PETM. Clay mineral distribution from sediments with non-hyperthermal and no or limited soil development (a) and mediate - well soil development (b) showing on average an increasing trend of smectite and decreasing trend of mixed-layer illite-smectite (I—S) dependent on median grain size. Samples from outsides the PETM (c) and within the PETM (d) both showing insignificant changes of smectites and other clay minerals with SDI. (e) Clay mineral distributions of samples from Pre-PETM, PETM, Post-PETM and Pre-ETM2 showing higher smectite and lower mixed-layer illite-smectite during the PETM compared to the Pre-PETM, Post-PETM, and Pre-ETM2. (f) Differences of proportions of clay minerals among Pre-PETM, Post-PETM, and Pre-ETM2 compared to the PETM. Clay mineralogical data of Pre-ETM2 is from Wang et al. (2017). The *p* value is the Pearson correlation coefficient of ANOVA, which denotes to be no difference if the $p > 0.05$ and be significant difference if the $p < 0.05$.

and relative stable sedimentation rate during and outside the PETM (Van der Meulen et al., 2020).

Diagenesis is interpreted to have had a limited effect on clay mineral composition in the Polecat Bench section. Clay minerals are sensitive to diagenesis because of smectite illitization (Bethke et al., 1986; Lanson et al., 2009). Smectite-bearing clay assemblage would generate highly illitic, ordered I/S and abundant discrete illite during diagenesis (Lanson et al., 2009). This is not observed in our samples. Illite shows low abundances of circa (6%) and displays irregular rather than regular I/S clays structures, which does not point to smectite illitization during diagenesis. Moreover, smectite has thought to transform to illite initially at temperatures ranging from 58 to 92 °C and completely spanning the 88–142 °C temperature range (Freed and Peacor, 1989). However, paleotemperature reconstructions yield maximum temperatures of <60 °C in the early Paleocene based on clumped isotope (Δ47) thermometry of spar carbonates (Snell et al., 2013) and oxygen isotope of fracture spar hematite (Bao et al., 1998), again not in line with clay mineral changes due to diagenesis.

The textures of the sediments and the morphologies and proportions of minerals in the PCB section indicate a detrital origin of the clay minerals. Sub-angular to sub-rounded mineral particles and randomly settled clay minerals reveal a characteristic of transported and

physically-weathered debris (Fig. 4A, B). Most smectites as well as micas in our samples occur as thin flakes that are a typical characteristic of breakage during transport, in line with a detrital origin (Fig. 4C, D). The characteristics of mineral textures and morphologies observed here are the same as we observed in the sediments across the ETM2 and H2 in the Deer Creek area around 15 km south of Polecat Bench also in the northern Bighorn Basin (Wang et al., 2017), indicating they likely shared similar a provenance and detrital origin.

Grain-size sorting played an important role in clay mineral proportions in Bighorn Basin fluvial sediments. Significant grain-size sorting of smectites was observed with smectites enriched in coarse-grained sediments (Fig. 6a, b), both in samples that underwent limited to intermediate pedogenesis and in samples showing intensive post-depositional pedogenesis. These findings are in line with semi-quantitative data from Wang et al. (2017) where their grain sizes distributions were obtained from field descriptions rather than laser particles analysis as in the current study. The smectite distribution dependence on grain size could largely be attributed to the hydrodynamical forces during the transportation and surface electrochemical characteristics of the smectite (Wang et al., 2017). In the channel environment, the small grain size and flake shape of smectite would quicker float and be transported than other clay minerals. To the floodplain environments studied here, regular overbank and crevasse flooding would bring in more smectite. The smectite will be further sorted, as smectite tends to flocculate more because of its high charge characteristic. Therefore smectite is logically enriched in coarser sediments. The scattered clay mineral proportions in the floodplain stratigraphic records is likely partly related to this grain-size sorting. Variable river hydrodynamics and soil hydrology can generate a variable distribution of sediments over the floodplains (Komar, 2007; Barefoot et al., 2022). Both authigenic mineral formation and autogenic recycling of basinal and catchment soils are other important factors driving the observed variability (Fig. 4f; Ramos et al., 2022).

5.2. Weathering changes during the PETM

Proportions of clay minerals in the basinal floodplains of the Bighorn Basin could be affected by climate-driven changes of physical and chemical weathering and erosive fluxes of weathering products. Chemical weathering would generate the breakdown and dissolving of parent silicates, followed by the neoformation of clay minerals (Barnhisel and Rich, 1967). Temperature and rainfall are two key climate factors promoting the weathering rate (White and Blum, 1995), together with time, pH, and soil p_{CO2} (Grant, 1969; White and Brantley, 2003; Winnick and Maher, 2008).

Chemical weathering in general would facilitate the neoformation and/or transformation of clay minerals in situ during pedogenesis (Wilson, 1999; Hong et al., 2012a; Yin et al., 2013). The degraded transformation with depletion of K and concomitant decrease of layer charge would proceed the transformation from illite to vermiculite, and then to smectite (Wilson, 1999), even though different pathways from illite to vermiculite and vermiculite to smectite were proposed (Chamley, 1989).

The clay mineral impact of in-situ pedogenesis is minimal and similar within and outside the PETM (Fig. 6c and d) with an insignificant decrease in smectite and increase in illite-smectite. These results are in line with those of Wang et al. (2017) studying younger parts of the Bighorn Basin floodplain record in the Deer Creek area. Soils are a very distinct character of the Fort Union and Willwood formations. The PETM is characterized by even more pronounced, thick, and well-developed paleosoils (Kraus and Riggins, 2007; Kraus et al., 2015). Despite these remarkable, macroscopic and microscopic pedogenic changes, also within the PETM, time for soil formation was apparently too short to significantly alter clay mineralogy. In the PCB section, three to four paleosols developed in one precession-driven overbank-avulsion cycle of ~21 kyr (Van der Meulen et al., 2020). One paleosol would thus have experienced some amount of weathering not more than up to 5–8 kyr before being buried by subsequent sedimentation. The process of chemical weathering from silicates to clay minerals will take several thousands of years up to millions of years according to for laboratory-derived chemical weathering rates (Price et al., 2005; White and Brantley, 2003). Such time scales are much longer than the average duration of the formation of an individual soil profile. Post-depositional pedogensis could thus not significantly alter mineralogy of the floodplain sediments in the Bighorn Basin.

In-situ pedogenesis is not the reason for the increase of smectites during the PETM. This was also found for the subsequent ETM2 hyperthermal (Wang et al., 2017). Increased physical weathering and erosion on the other hand could be the cause of the smectite increase during the PETM. Factors including tectonic activity and climate change driving hydrological conditions and transportation may control detrital clay mineral assemblages and proportions (Hong et al., 2012b; Liu et al., 2016; Zhao et al., 2018). Tectonic activity can affect the clay mineral assemblages and proportions by intensifying the denudation and recycling of parent rocks from the hinterland, while this process is anticipated to have an impact at relatively long time scales (eg. Hong et al., 2010, 2012b). No change in provenance has been observed across the Fort Union to Willwood formations and so tectonics are not related to the shifts in clay mineralogy during the PETM (May et al., 2013; Welch et al., 2022).

Climate-driven hydrological condition and transportation would change the clay mineral assemblages and proportions at shorter terms (Liu et al., 2003; Zhang et al., 2020). Lines of local evidence such as paleosol morphology, fluvial deposits and style, ichnofossils and plant and mammal fossils have documented the Bighorn Basin indicating a seasonally drier, much hotter, and more abundant high discharge regimes during the PETM (Kraus and Hasiotis, 2006; Smith et al., 2008; Kraus et al., 2013, Foreman, 2014; Kraus et al., 2015; Westerhold et al., 2018). Leaf area, leaf-wax n-alkane δD and *Coryphodon* $\delta^{18}O$ data also indicated that precipitation may have declined (Fricke et al., 1998; Wing et al., 2005; Baczynski et al., 2017).

The increased summer temperatures and enhanced dry seasons during the PETM could have caused less dense vegetation covers rooting soils both in the catchments and the basin. This would have reduced cohesiveness of upstream laterites and basinal overbank sediments as suggested by Foreman (2014) based on fluvial channel sandbody studies (Fig. 7). An increase in storminess (Camichael et al., 2018) may have accelerated the reworking and erosion of the previously deposited more proximal sediments (Foreman, 2014). Along the basin margins there Cretaceous shales and bentonites as evidenced by an immobile element mixing model (Ramos et al., 2022) and fossil n-alkanes analysis (Baczynski et al., 2017). The abundant Cretaceous bentonites were deposited from the Aptian to Turonian and from the Campanian to the end of the Cretaceous (Hannon et al., 2019, 2020). These could have provided potential sources for the detrital smectites. Lithological description of Cretaceous strata showed that bentonites were preserved in almost all the sedimentary units except for Muddy Sandstone (Supplementary table 1). Mineralogical analyses of shales and bentonites indicated smectite and I/S dominated clay mineral compositions in bulk rock, besides illite and kaolinite. As smectite tends to be rich in smaller grain size, smectite-rich (95% $<$ 2 μm) Cretaceous bentonites (Fitzsimmons and Johnson, 2000; Chipera and Bish, 2001) may have flushed downstream and these bentonites could be easier to be affected by the pore-water pressure variability thus losing the cohesive strength compared to other source rocks, such as limestone, dolostone, sandstone, granite, and gneiss that made up the remainder of the catchments (Neasham and Vondra, 1972). Moreover, repeated stormy events, longer summer droughts, a lower vegetation density may have favoured enhanced physical weathering and erosion during the PETM event bringing in smectite-rich sediments.

The full clay mineral changes in the PETM seem to be reached in the second precession-driven overbank-avulsion cycle in the event. This is

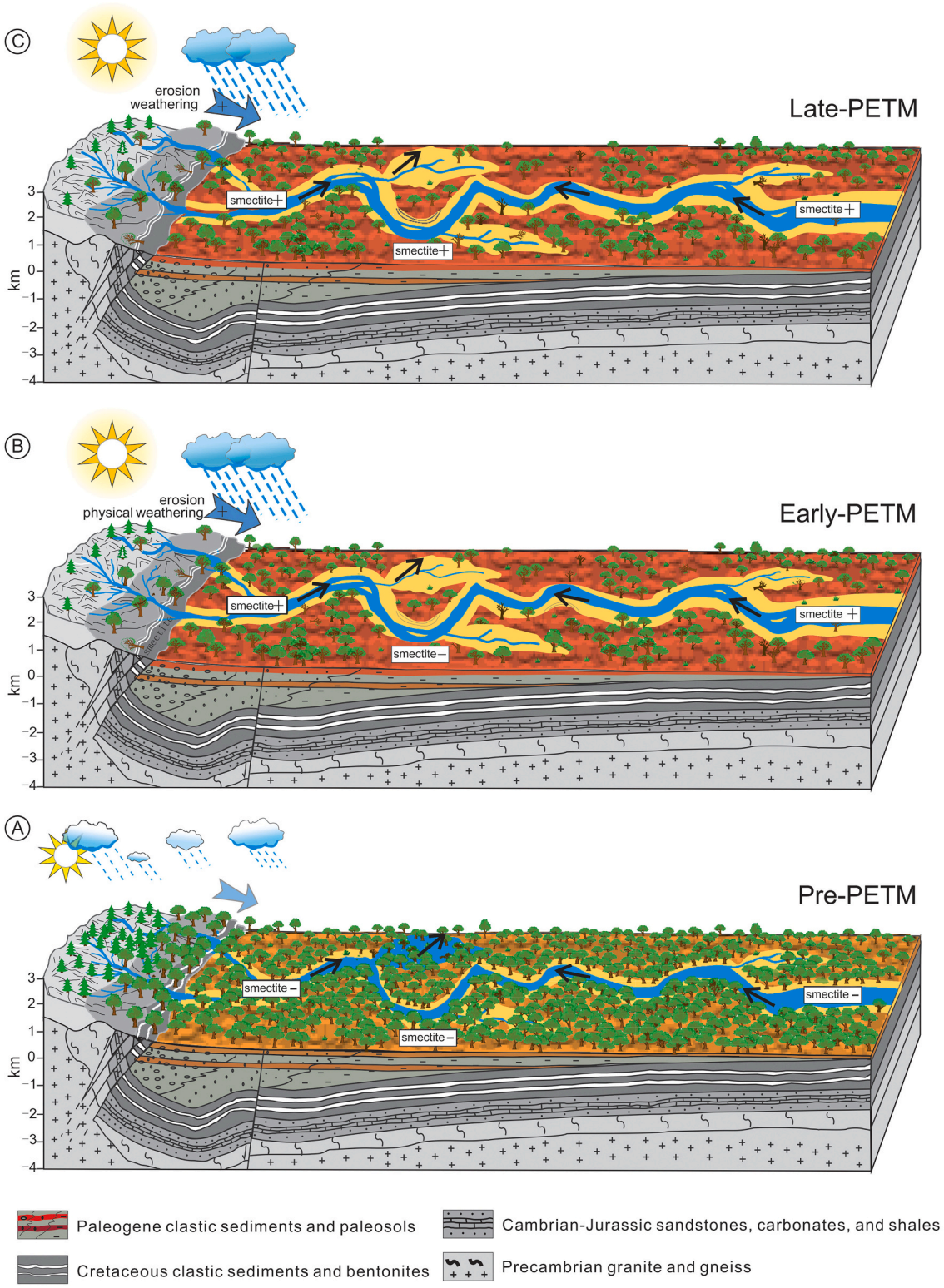

Fig. 7. Paleocene-Eocene landscapes in the Bighorn Basin, Wyoming, showing the spatial distribution of smectite across the basin through the PETM. View is to the north, with stream input from adjacent highlands on the western margin and distal highlands much farther to the east. The increase in smectite through the PETM is attributed to enhanced physical weathering of Cretaceous bentonites on the basin margins during the PETM. The black arrows denote the directions of water flow. The water finally flows to the north.

more than ~21 kyr after the main onset of the PETM. Temperature reconstructions show immediate warming in the early PETM (Frieling et al., 2019) and different early PETM climates compared to middle and late PETM climates. This would not explain the seemingly lagged response of clay minerals to the onset (Fig. 7). Instead, we attribute to lagged response to signal shredding in the source-to-sink system.

Studies of source-to-sink transport processes of fluvial sediments have documented that the lag time varies in different river conditions

with different local divergence of sediment-transport capacity depending on channel gradient, river length, and sediment transport influx (Macklin et al., 2002; Goldberg et al., 2021; Wang et al., 2022b). In general, rivers with moderate sediments transport influx could have the lag time of hundreds to thousands years (Macklin et al., 2002), while lower sediments transport influx increases the lag time in terraces, as long as thousands years, in response to climate (Hancock and Anderson, 2002).

After the onset of the PETM, climatic change led to increased amounts of smectite eroding Cretaceous bentonites. The river waters would relatively rapidly be filled with smectite-enriched suspended load early on in the PETM body. However, the river channels are constantly moving and eroding through the adjacent floodplains. In the early PETM, the channels were moving in floodplain sediments deposited during pre-PETM times that had lower smectite contents. This causes the downstream river waters to be more and more a mix of smectite-enriched catchment waters and smectite-poor floodplains sediments. The floodplains will continuously aggrade particularly during phases of regional-scale river avulsion paced by climatic precession (Abels et al., 2013). It will thus logically take at least one precession cycle after the PETM onset before most of the pre-PETM, lower-smectite signal disappeared from the basinal floodplain sediments. That left behind smectite-enriched river waters mixing with more and more smectite-rich river floodplains (Fig. 7).

Interestingly, the mixing of smectite-enriched catchment waters with smectite-poor basinal sediments during the early PETM, would produce increased scatter of clay mineral composition in Polecat Bench floodplains during the early PETM. This is because individual sediment pulses may occasionally be mostly sourced directly in the catchment or mixing catchment with basinal floodplain signals. And, it is expected that this scatter consists of the end-member clay mineral compositions of both the smectite-enriched catchment and smectite-poor basinal floodplain sediments. The bins related to cycles −1, 0 and 1 around the PETM onset do indeed show an increased scatter of illite-smectite and smectite and values generally do not exceed nor minimal and maximal values of pre-PETM and PETM in both records (Fig. 5).

The prolonged nature of the smectite enrichment after the PETM event may relate to post-PETM signal propagation times that are even longer than in the PETM body due to lower recycling rates and so longer signal shredding rates after the event. Reduced storminess and increased overbank cohesiveness drives slower post-PETM signal propagation, while comparison with pre-ETM2 data from the northern Bighorn Basin shows that smectite and I/S do return to approximate pre-PETM values eventually (Wang et al., 2017; Fig. 5). Ideally, one would wish to know how clay minerals responded in the period between 200 and 500 kyr from the onset to know how quickly pre-PETM values were reached. Producing those records would be well beyond the scope of this study, not in the last place because it would require extending the section upwards in the Sand Coulee area rather than Polecat Bench, as the PCB section has limited further upward extend (Van der Meulen et al., 2020).

Clay mineralogical study of PETM sections that are located closer to the basin margins are worth further investigation. Shorter distances from the basin margins would imply shorter signal shredding both for the PETM onset lag-time of smectite-enrichment and for the post-PETM recovery. Such a study could corroborate the current interpretation, while it can be only done using high-resolution floodplain clay mineralogical records as variability is too large to evaluate low-resolution clay mineral records from alluvial records.

Pre-PETM values are comparable to pre-ETM2 values (Fig. 5). In the early Eocene, long-term trends are expected both in climate and tectonic changes on top of the short-term precession-cycle climate changes and the hyperthermal events. In fact, I/S values in pre-ETM2 are higher than pre-PETM and particularly smectite and chlorite are slightly lower, with illite and kaolinite values are similar. The overall similar clay mineral values, except for smectite and I/S, between pre-PETM and pre-ETM2 could be indicate relatively stable source rocks and similar depositional environments in the Bighorn Basin during the time. The increase of I/S could relate to persistent erosion of diagenetic Cretaceous shales that likely contain higher amounts of I/S when deeper buried rocks are weathered, such as in the Cody shale (Supplement table 1). The Cretaceous Mowry shales in the Denver Basin observed a higher illite layers in I/S with increasing depths of burial (Elliott et al., 1991), supporting the burial diagenesis could have took place in the Cretaceous strata.

The onset of the PETM is shown to be preceded by pre-onset climate change (Secord et al., 2012; Sluijs et al., 2007). The clay mineralogical records produced here suggest a slight trend from cycle −7 to −1 along with an increase in variability, both in smectite and I/S. The more pronounced increase in clay abundance variability starts at cycle −1 rather than at the onset. This suggests that climate change related to the PETM started well before the event in line with other records from the basin and the marine realm (Secord et al., 2012; Sluijs et al., 2007; Van der Meulen et al., 2020).

5.3. Implication of observed weathering changes during the PETM

We interpret the significant and lagged increases of smectites during the PETM in the Bighorn Basin basinal floodplains as a result of enhanced physical weathering and erosion rather than chemical weathering related to reduced vegetation covers and increased storminess during the event. Our interpretation is consistent with local records indicating strong reworking and erosion during the Paleogene in the Bighorn Basin (May et al., 2013; Foreman, 2014; Baczynski et al., 2017, 2019; Welch et al., 2022). Similar interpretations of enhanced climate seasonality with physical weathering and erosion are observed in records of shallow marine deposits (Schmitz and Pujalte, 2003, 2007; Sluijs et al., 2008; John et al., 2012; Pogge von Strandmann et al., 2021). The increase in smectite-supply in the Polecat Bench section coincides with the increases of allochthonous carbon in more southern sections of the Bighorn Basin (Baczynski et al., 2017, 2019). This supports enhanced physical weathering and erosion fluxes to the basin with signal shredding and lag time of this signal due to the sediment recycling within the more proximal, basinal floodplains.

This lagged and prolonged physical weathering and erosion signal may be in line with similarly lagged and prolonged f_{shale} and δ^7Li values of clay fractions (< 2 μm) at the Polecat Bench during the PETM (Ramos et al., 2022). These authors relate this to intensified chemical weathering, despite the clay fractions were detrital in origin. The δ^7Li values decrease within ~7 kyr of the PETM onset (Ramos et al., 2022), faster than the ~21 kyr respond of smectite increases here. Both differences in weathering type and lagged time between clay mineral and Li isotope records could attribute to the different sensitivity of δ^7 Li values of clay fractions and clay minerals to chemical weathering. At the same time, the δ^7 Li values of clay fractions could have shorter response times to chemical weathering than clay mineral assemblages, because Li as a mobile element can migrate from silicates to solution in hundreds of days without a change of mineral phases (Pogge von Strandmann et al., 2019). Clay mineral assemblages (<2 μm) could be depositing in accumulative floodplain environment with limited time for weathering, which has limitation when tracing the chemical weathering in this short-term hyperthermal. Detailed clay mineralogy for individual paleosols spanning the PETM on grain size fractions below 1 μm would deserve further investigation as authigenic minerals are observed at these scales (Fig. 4F).

Clechenko et al. (2007) reported high abundances of kaolinite during the PETM interpreted to be caused by enhanced pedogenesis in the Williston Basin, North Dokoka, USA. This could suggest the Bighorn and Williston Basins had contrasting weathering impacts during the PETM, or that the origin of this kaolinite increase needs to be further investigated as it could also be driven by increased physical weathering and erosion of local, kaolinite-rich catchment rocks.

Our data suggest an enhanced physical weathering and erosion

resulting in increased sediment fluxes to the basins possibly supporting the hypothesis of enhanced carbon burial playing a more important role in carbon sequestration than silicate weathering for the relatively short-term hyperthermals. It seem counterintuitive that the strong climatic changes during the PETM did not a chemically alter catchment and basinal sediments. It could be that in settings where erosion may have been less strongly affecting catchment laterites, enhanced chemical weathering may still have played a significant role.

6. Conclusion

Clay mineral assemblages of the floodplain sediments in the Polecat bench section of the northern Bighorn Basin in Wyoming, USA, reveal that smectite was the dominant clay mineral species with minor contributions of mixed-layer illite-smectite and kaolinite. Grain-size sorting had a significant impact on clay mineral distributions in these fluvial environments. In-situ, post-depositional pedogenesis had a marginal impact on clay mineralogy of the floodplains likely due to too short formation times of the paleosoils. A substantial increase in smectite and decrease in I/S occurs in response to climate change related to the PETM. We find that these clay mineral changes are unrelated to grain size and in-situ pedogenic changes as these effects remain stable across the PETM. Clay morphology analysis corroborates that these minerals are primarily of detrital origin in these records including during the PETM. We therefore interpret the clay mineral changes to relate to enhanced physical weathering and erosion of Cretaceous bentonites due to increase temperatures, dryness and storminess of climates and related decrease of vegetation cover. The lagged response after the onset of the PETM and prolonged response after the recovery of the PETM may relate to signal shredding within the basin. As soon as climate changes after the onset of the PETM, catchment waters may enriched river waters with smectites. However, river channels continuously erode surrounding floodplain sediments that in the early PETM still had the pre-PETM smectite-poor signal. It apparently took at least 21-kyr before the full signal was propagated to the basinal setting studied here. After the PETM event, reduced hydrological cycle may have even slowed down signal propagation times such to causes an even longer delay time before full post-PETM signals were reached. Our data suggest an enhanced physical weathering and erosion resulting in increased sediment fluxes to the basins. It could be that in settings where erosion may have been less strongly affecting catchment laterites, enhanced chemical weathering may still have played a significant role.

Author contributions

The study was designed by CW, HH and HA. Sample and data were collected by KJ, CW, CZ, YX, MP, and HA. Data analysis and the interpretation of results was completed by CW, KY, BS, LJ, PG, MP and HA. Draft manuscript preparation and editing was completed by KJ, CW, and HA. All authors reviewed the results and approved the final version of the paper.

Declaration of Competing Interest

The authors declare that they have no known competing financial interests or personal relationships that could have appeared to influence the work reported in this paper.

Data availability

The data that has been used is confidential.

Acknowledgments

We appreciate the editor Dr. Alex Dickson for the editorial handling and Dr. Evan, J. Ramos and an anonymous reviewer for their constructive comments. We thank Mr. Clinton van de Ven and Mr. Haiyang Liu for the assistances on the grain size and XRD analyses, respectively. We acknowledge Mr. Timothy Baars, Dr. Qian Fang, Dr. Liulin Chen, MS. Chen Liu, and Dr. Lijun Wang on constructive comments for the draft. We would like to be grateful for the grants from National Natural Science Foundation of China (Nos. 42072056, 42172045, 41772032, 41602037 and 41972040) and partially an NWO-ALW VENI grant to HAA (project number 863.11.006). Chaowen Wang acknowledges the grant from Chinese Scholarship Council (CSC) to support him as a visiting scholar in TU Delft.

Appendix A. Supplementary data

Supplementary data to this article can be found online at https://doi.org/10.1016/j.palaeo.2023.111445.

References

Abels, H.A., Clyde, W.C., Gingerich, P.D., Hilgen, F.J., Fricke, H.C., Bowen, G.J., Lourens, L.J., 2012. Terrestrial carbon isotope excursions and biotic change during Palaeogene hyperthermals. Nat. Geosci. 5, 326–329.
Abels, H.A., Kraus, M.J., Gingerich, P.D., 2013. Precession-scale cyclicity in the fluvial lower Eocene Willwood Formation of the Bighorn Basin, Wyoming (USA). Sedimentology 60, 1467–1483.
Abels, H.A., Lauretano, V., Van Yperen, A.E., Hopman, T., Zachos, J.C., Lourens, L.J., Gingerich, P.D., Bowen, G.J., 2016. Environmental impact and magnitude of paleosol carbonate carbon isotope excursions marking five early Eocene hyperthermals in the Bighorn Basin, Wyoming. Clim. Past 12, 1151–1163.
Baczynski, A.A., McInerney, F.A., Wing, S.L., Kraus, M.J., Bloch, J.I., Secord, R., 2017. Constraining paleohydrologic change during the Paleocene-Eocene thermal Maximum in the continental interior of North America. Palaeogeogr. Palaeoclimatol. Palaeoecol. 465, 237–246.
Baczynski, A.A., McInerney, F.A., Freeman, K.H., Wing, S.L., 2019. Carbon isotope record of trace n-alkanes in a continental PETM section recovered by the Bighorn Basin Coring Project (BBCP). Paleoceanogr. Paleoclimatol. 34, 853–865.
Bao, H., Koch, P.L., Hepple, R.P., 1998. Hematite and calcite coatings on fossil vertebrates. J. Sediment. Res. 68, 727–738.
Barefoot, E.A., Nittrouer, J.A., Foreman, B.Z., Hajek, E.A., Dickens, G.R., Baisden, T., Toms, L., 2022. Evidence for enhanced fluvial channel mobility and fine sediment export due to precipitation seasonality during the Paleocene-Eocene thermal maximum. Geology 50, 116–120.
Barnhisel, R., Rich, C., 1967. Clay mineral formation in different rock types of a weathering boulder conglomerate. Soil Sci. Soc. Am. J. 31, 627–631.
Bethke, C.M., Vergo, N., Altaner, S.P., 1986. Pathways of smectite illitization. Clay Clay Miner. 34, 125–135.
Bolle, M.P., Adatte, T., 2001. Palaeocene-early Eocene climatic evolution in the Tethyan realm: clay mineral evidence. Clay Miner. 36, 249–261.
Bowen, G.J., Zachos, J.C., 2010. Rapid carbon sequestration at the termination of the Palaeocene-Eocene thermal Maximum. Nat. Geosci. 3, 866–869.
Bowen, G.J., Koch, P.L., Gingerich, P.D., Norris, R.D., Bains, S., Corfield, R.M., 2001. Refined isotope stratigraphy across the continental Paleocene-Eocene boundary on Polecat Bench in the northern Bighorn Basin. In: Gingerich, P.D. (Ed.), Paleocene-Eocene Stratigraphy and Biotic Change in the Bighorn and Clarks Fork Basins, Wyoming, 33. University of Michigan Papers on Paleontology, pp. 73–88.
Bralower, T.J., Kump, L.R., Self-Trail, J.M., Robinson, M.M., Lyons, S., Babila, T., Ballaron, E., Freeman, K.H., Hajek, E., Rush, W., 2018. Evidence for shelf acidification during the onset of the Paleocene-Eocene thermal maximum. Paleoceanogr. Paleoclimatol. 33, 1408–1426.
Camichael, M., Pancost, R.D., Lunt, D.J., 2018. Changes in the occurrence of extreme precipitation events at the Paleocene-Eocene thermal maximum. Earth Planet. Sci. Lett. 501, 24–36.
Chamley, H., 1989. Clay mineralogy. Springer-Verlag, Heidelberg.
Chipera, S.J., Bish, D.L., 2001. Baseline studies of the clay minerals society source clays: powder X-ray diffraction analyses. Clay Clay Miner. 49, 398–409.
Clechenko, E.R., Kelly, D.C., Harrington, G.J., Stiles, C.A., 2007. Terrestrial records of a regional weathering profile at the Paleocene-Eocene boundary in the Williston Basin of North Dakota. Geol. Soc. Am. Bull. 119, 428–442.
Clyde, W.C., Gingerich, P.D., 1998. Mammalian community response to the latest Paleocene thermal maximum: an isotaphonomic study in the northern Bighorn Basin, Wyoming. Geology 26, 1011–1014.
Dypvik, H., Riber, L., Burca, F., Rüther, D., Jargvoll, D., Nagy, J., Jochmann, M., 2011. The Paleocene-Eocene thermal maximum (PETM) in Svalbard—clay mineral and geochemical signals. Palaeogeogr. Palaeoclimatol. Palaeoecol. 302, 156–169.
Elliott, W.C., Aronson, J.L., Matisoff, G., Gautier, D.L., 1991. Kinetics of the smectite to illite transformation in the Denver Basin: Clay mineral, K-Ar data, and mathematical model results. Am. Assoc. Petrol. Geol. Bull. 75, 436–462.
Fan, M., Carrapa, B., 2014. Late Cretaceous–early Eocene Laramide uplift, exhumation, and basin subsidence in Wyoming: Crustal responses to flat slab subduction. Tectonics 33, 509–529.
Fanshawe, J.R., 1971. Structural evolution of big Horn basin. In: , 23. Guidebook-Wyoming Geological Association, pp. 35–37.

Fitzsimmons, R., Johnson, S., 2000. Forced regressions: recognition, architecture and genesis in the Campanian of the Bighorn Basin, Wyoming. Geol. Soc. Lond. Spec. Publ. 172, 113–139.
Foreman, B.Z., 2014. Climate-driven generation of a fluvial sheet sand body at the Paleocene-Eocene boundary in north-West Wyoming (USA). Basin Res. 26, 225–241.
Foreman, B.Z., Heller, P.L., Clementz, M.T., 2012. Fluvial response to abrupt global warming at the Palaeocene/Eocene boundary. Nature 491, 92–95.
Freed, R.L., Peacor, D.R., 1989. Variability in temperature of the smectite/illite reaction in Gulf Coast sediments. Clay Miner. 24, 171–180.
Fricke, H.C., Clyde, W.C., O'Neil, J.R., 1998. Intra-tooth variations in δ18O (PO4) of mammalian tooth enamel as a record of seasonal variations in continental climate variables. Geochim. Cosmochim. Acta 62, 1839–1850.
Frieling, J., Peterse, F., Lunt, D.J., Bohaty, S.M., Sinninghe Damste, J.S., Reichart, G.J., Sluijs, A., 2019. Widespread warming before and elevated barium Burial during the Paleocene-Eocene thermal Maximum: evidence for methane hydrate release? Paleoceanogr. Paleoclimatol. 34, 546–566.
Gibson, T.G., Bybell, L.M., Mason, D., 2000. Stratigraphic and climatic implications of clay mineral changes around the Paleocene/Eocene boundary of the northeastern US margin. Sediment. Geol. 134, 65–92.
Gibson, T.G., Bybell, L.M., Owens, J.P., 1993. Latest Paleocene lithologic and biotic events in neritic deposits of southwestern New Jersey. Paleoceanography 8, 495–514.
Gingerich, P.D., 2003. Mammalian responses to climate change at the Paleocene-Eocene boundary: Polecat Bench. Geol. Soc. Am. Spec. Pap. 369, 463–478.
Giusberti, L., Rio, D., Agnini, C., Backman, J., Fornaciari, E., Tateo, F., Oddone, M., 2007. Mode and tempo of the Paleocene-Eocene thermal maximum in an expanded section from the venetian pre-Alps. Geol. Soc. Am. Bull. 119, 391–412.
Goldberg, S.L., Schmidt, M.J., Perron, J.T., 2021. Fast response of Amazon rivers to Quaternary climate cycles. J. Geophys. Res. Earth Surf. 126, 1–17.
Grant, W.H., 1969. Abrasion pH, an index of chemical weathering. Clay Clay Miner. 17, 151–155.
Gutjahr, M., Ridgwell, A., Sexton, P.F., Anagnostou, E., Pearson, P.N., Pälike, H., Norris, R.D., Thomas, E., Foster, G.L., 2017. Very large release of mostly volcanic carbon during the Palaeocene-Eocene thermal Maximum. Nature 548, 573–577.
Hancock, G.S., Anderson, R.S., 2002. Numerical modeling of fluvial strath-terrace formation in response to oscillating climate. Geol. Soc. Am. Bull. 114, 1131–1142.
Handley, L., O'Halloran, A., Pearson, P.N., Hawkins, E., Nicholas, C.J., Schouten, S., McMillan, I.K., Pancost, R.D., 2012. Changes in the hydrological cycle in tropical East Africa during the Paleocene-Eocene thermal Maximum. Palaeogeogr. Palaeoclimatol. Palaeoecol. 329, 10–21.
Hannon, J.S., Dietsch, C., Huff, W.D., 2020. Trace-element and Sr and Nd isotopic geochemistry of cretaceous bentonites in Wyoming and South Dakota tracks magmatic processes during eastward migration of Farallon arc plutons. Geol. Soc. Am. Bull. 133 (7–8), 1542–1559.
Hannon, J.S., Huff, W.D., Sturmer, D.M., 2019. Geochemical relationships in cretaceous bentonites as inferred from linear discriminant analysis. Sedimentary Geolgy 390, 1–14.
Hong, H., Churchman, G.J., Gu, Y., Yin, K., Wang, C., 2012a. Kaolinite–smectite mixed-layer clays in the Jiujiang red soils and their climate significance. Geoderma 173, 75–83.
Hong, H., Wang, C., Zeng, K., Zhang, K., Yin, K., Li, Z., 2012b. Clay mineralogy of the Zhada sediments: evidence for climatic and tectonic evolution since~ 9 Ma in Zhada, southwestern Tibet. Clay Clay Miner. 60, 240–253.
Hong, H., Zhang, K., Li, Z., 2010. Climatic and tectonic uplift evolution since ~ 7 Ma in Gyirong basin, southwestern Tibet plateau: clay mineral evidence. Int. J. Earth Sci. 99, 1305–1315.
Inglis, G.N., Bragg, F., Burls, N.J., Cramwinckel, M.J., Evans, D., Foster, G.L., Huber, M., Lunt, D.J., Siler, N., Steinig, S., 2020. Global mean surface temperature and climate sensitivity of the early Eocene Climatic Optimum (EECO), Paleocene-Eocene thermal Maximum (PETM), and latest Paleocene. Clim. Past 16, 1953–1968.
Jackson, M.L., 1975. Soil chemical analysis–Advanced Course, 2nd ed. Published by the author, University of Wisconsin, Madison, Wisconsin.
John, C.M., Banerjee, N.R., Longstaffe, F.J., Sica, C., Law, K.R., Zachos, J.C., 2012. Clay assemblage and oxygen isotopic constraints on the weathering response to the Paleocene-Eocene thermal maximum, east coast of North America. Geology 40, 591–594.
Kennett, J.P., Stott, L., 1991. Abrupt deep-sea warming, palaeoceanographic changes and benthic extinctions at the end of the Palaeocene. Nature 353, 225–229.
Knighton, A.D., 1999. Downstream variation in stream power. Geomorphology 29, 293–306.
Koch, P.L., Zachos, J.C., Gingerich, P.D., 1992. Correlation between isotope records in marine and continental carbon reservoirs near the Palaeocene/Eocene boundary. Nature 358, 319–322.
Komar, P., 2007. Chapter 1: The entrainment, transport and sorting of heavy minerals by waves and currents. Dev. Sedimentol. 58, 3–48.
Konert, M., Vandenberghe, J., 1997. Comparison of laser grain size analysis with pipette and sieve analysis: a solution for the underestimation of the clay fraction. Sedimentology 44, 523–535.
Kraus, M.J., 1998. Development of potential acid sulfate paleosols in Paleocene floodplains, Bighorn Basin, Wyoming, USA. Palaeogeogr. Palaeoclimatol. Palaeoecol. 144, 203–224.
Kraus, M.J., Gwinn, B., 1997. Facies and facies architecture of Paleogene floodplain deposits, Willwood Formation, Bighorn basin, Wyoming, USA. Sediment. Geol. 114, 33–54.
Kraus, M.J., Hasiotis, S.T., 2006. Significance of different modes of rhizolith preservation to interpreting paleoenvironmental and paleohydrologic settings: examples from Paleogene paleosols, Bighorn Basin, Wyoming, USA. J. Sediment. Res. 76, 633–646.
Kraus, M.J., McInerney, F.A., Wing, S.L., Secord, R., Baczynski, A.A., Bloch, J.I., 2013. Paleohydrologic response to continental warming during the Paleocene-Eocene thermal maximum, Bighorn Basin, Wyoming. Palaeogeogr. Palaeoclimatol. Palaeoecol. 370, 196–208.
Kraus, M.J., Riggins, S., 2007. Transient drying during the Paleocene-Eocene thermal Maximum (PETM): analysis of paleosols in the Bighorn Basin, Wyoming. Palaeogeogr. Palaeoclimatol. Palaeoecol. 245, 444–461.
Kraus, M.J., Woody, D.T., Smith, J.J., Dukic, V., 2015. Alluvial response to the Paleocene-Eocene thermal maximum climatic event, polecat bench, Wyoming (USA). Palaeogeogr. Palaeoclimatol. Palaeoecol. 435, 177–192.
Lanson, B., Sakharov, B.A., Claret, F., Drits, V.A., 2009. Diagenetic smectite-to-illite transition in clay-rich sediments: a reappraisal of X-ray diffraction results using the multi-specimen method. Am. J. Sci. 309, 476–516.
Liu, Z., Trentesaux, A., Clemens, S.C., Colin, C., Wang, P., Huang, B., Boulay, S., 2003. Clay mineral assemblages in the northern South China Sea: implications for East asian monsoon evolution over the past 2 million years. Mar. Geol. 201, 133–146.
Liu, Z., Zhao, Y., Colin, C., Stattegger, K., Wiesner, M.G., Huh, C.-A., Zhang, Y., Li, X., Sompongchaiyakul, P., You, C.-F., 2016. Source-to-sink transport processes of fluvial sediments in the South China Sea. Earth Sci. Rev. 153, 238–273.
Lourens, L.J., Sluijs, A., Kroon, D., Zachos, J.C., Thomas, E., Röhl, U., Bowles, J., Raffi, I., 2005. Astronomical pacing of late Palaeocene to early Eocene global warming events. Nautre 435, 1083–1087.
Ma, Z., Gray, E., Thomas, E., Murphy, B., Zachos, J., Paytan, A., 2014. Carbon sequestration during the Palaeocene-Eocene thermal Maximum by an efficient biological pump. Nat. Geosci. 7, 382–388.
Macklin, M., Fuller, I., Lewin, J., Maas, G., Passmore, D., Rose, J., Woodward, J., Black, S., Hamlin, R., Rowan, J., 2002. Correlation of fluvial sequences in the Mediterranean basin over the last 200 ka and their relationship to climate change. Quat. Sci. Rev. 21, 1633–1641.
Magioncalda, R., Dupuis, C., Smith, T., Steurbaut, E., Ginerich, P.D., 2004. Paleocene-Eocene carbon isotope excursion in organic carbon and pedogenic carbonate: Direct comparison in a continental stratigraphic section. Geology 32, 553–556.
Malone, D.H., Craddock, J.P., Welch, J.L., Foreman, B.Z., 2017. Detrital zircon U-Pb geochronology and provenance of the Eocene Willwood Formation, northern Absaroka Basin, Wyoming.
May, S.R., Gray, G.G., Summa, L.L., Stewart, N.R., Gehrels, G.E., Pecha, M.E., 2013. Detrital zircon geochronology from the Bighorn Basin, Wyoming, USA: Implications for tectonostratigraphic evolution and paleogeography. Geol. Soc. Am. Bull. 125, 1403–1422.
McInerney, F.A., Wing, S.L., 2011. The Paleocene-Eocene thermal Maximum: a perturbation of carbon cycle, climate, and biosphere with implications for the future. Annu. Rev. Earth Planet. Sci. 39, 489–516.
Moore, D.M., Reynolds, R.C., 1997. X-ray Diffraction and the Identification and Analysis of Clay Minerals. Oxford University Press.
Murphy, B., Farley, K., Zachos, J., 2010. An extraterrestrial 3He-based timescale for the Paleocene-Eocene thermal maximum (PETM) from Walvis Ridge, IODP Site 1266. Geochim. Cosmochim. Acta 74, 5098–5108.
Neasham, J.W., Vondra, C.F., 1972. Stratigraphy and petrology of the lower Eocene Willwood Formation, Bighorn Basin, Wyoming. Geol. Soc. Am. Bull. 83, 2167–2180.
Omar, G.I., Lutz, T.M., Giegengack, R., 1994. Apatite fission-track evidence for Laramide and post-Laramide uplift and anomalous thermal regime at the Beartooth overthrust, Montana-Wyoming. Geol. Soc. Am. Bull. 106, 74–85.
Penman, D.E., Turner, S.K., Sexton, P.F., Norris, R.D., Dickson, A.J., Boulila, S., Ridgwell, A., Zeebe, R.E., Zachos, J.C., Cameron, A., 2016. An abyssal carbonate compensation depth overshoot in the aftermath of the Palaeocene-Eocene thermal Maximum. Nat. Geosci. 9, 575–580.
Pogge von Strandmann, P.A.E., Fraser, W.T., Hammond, S.J., Tarbuck, G., Wood, I.G., Oelkers, E.H., Murphy, M.J., 2019. Experimental determination of Li isotope behaviour during basalt weathering. Chem. Geol. 517, 34–43.
Pogge von Strandmann, P.A.E., Jones, M.T., Joshua West, A., Murphy, M.J., Stokke, E. W., Tarbuck, G., Wilson, D.J., Pearce, C.R., Schmidt, D.N., 2021. Lithium isotope evidence for enhanced weathering and erosion during the Paleocene-Eocene thermal Maximum. Science. Advances 7, eabh4224.
Price, J.R., Velbel, M.A., Patino, L.C., 2005. Rates and time scales of clay-mineral formation by weathering in saprolitic regoliths of the southern Appalachians from geochemical mass balance. Geol. Soc. Am. Bull. 117, 783–794.
Rad, S., Basile-Doelsch, I., Quesnel, F., Dupuis, C., 2009. Silicium isotopes as a proxy of weathering processes during the PETM. Goldschmidt Conf, Abst, A1066.
Ramos, E.J., Breecker, D.O., Barnes, J.D., Li, F., Gingerich, P.D., Loewy, S.L., Satkoski, A. M., Baczynski, A.A., Wing, S.L., Miller, N.R., 2022. Swift weathering response on floodplains during the Paleocene-Eocene thermal Maximum. Geophys. Res. Lett. 49, e2021GL097436.
Reynolds III, R., Reynolds Jr., R., 2012. NEWMOD II a computer program for the calculation of one-dimensional diffraction patterns of mixed-layered clays, 1526 Farlow Avenue. Crofton, MD 21114.
Robert, C., Kennett, J.P., 1994. Antarctic subtropical humid episode at the Paleocene-Eocene boundary: Clay-mineral evidence. Geology 22, 211–214.
Röhl, U., Westerhold, T., Bralower, T.J., Zachos, J.C., 2007. On the duration of the Paleocene-Eocene thermal maximum (PETM). Geochem. Geophys. Geosyst. 8.
Schmitz, B., Pujalte, V., 2003. Sea-level, humidity, and land-erosion records across the initial Eocene thermal maximum from a continental-marine transect in northern Spain. Geology 31, 689–692.

Schmitz, B., Pujalte, V., 2007. Abrupt increase in seasonal extreme precipitation at the Paleocene-Eocene boundary. Geology 35, 215–218.
Secord, R., Bloch, J.I., Chester, S.B., Boyer, D.M., Wood, A.R., Wing, S.L., Kraus, M.J., McInerney, F.A., Krigbaum, J., 2012. Evolution of the Earliest horses Driven by climate Change in the Paleocene-Eocene thermal Maximum. Science 335, 959–962.
Sluijs, A., Brinkhuis, H., Crouch, E.M., John, C.M., Handley, L., Munsterman, D., Bohaty, S.M., Zachos, J.C., Reichart, G.J., Schouten, S., 2008. Eustatic variations during the Paleocene-Eocene greenhouse world. Paleoceanography 23, PA4216.
Sluijs, A., Brinkhuis, H., Schouten, S., Bohaty, S.M., John, C.M., Zachos, J.C., Reichart, G., Sinninghe Damsté, J.S., Crouch, E.M., Dickens, G.R., 2007. Environmental precursors to rapid light carbon injection at the Palaeocene/Eocene boundary. Nature 450 (7173), 1218–1221.
Smith, J.J., Hasiotis, S.T., Woody, D.T., Kraus, M.J., 2008. Paleoclimatic implications of crayfish-mediated prismatic structures in paleosols of the Paleogene Willwood Formation, Bighorn Basin, Wyoming, USA. J. Sediment. Res. 78, 323–334.
Snell, K.E., Thrasher, B.L., Eiler, J.M., Koch, P.L., Sloan, L.C., Tabor, N.J., 2013. Hot summers in the Bighorn Basin during the early Paleogene. Geology 41, 55–58.
Soliman, M.F., Aubry, M.-P., Schmitz, B., Sherrell, R.M., 2011. Enhanced coastal paleoproductivity and nutrient supply in Upper Egypt during the Paleocene/Eocene thermal Maximum (PETM): Mineralogical and geochemical evidence. Palaeogeogr. Palaeoclimatol. Palaeoecol. 310, 365–377.
Thomas, L.E., 1965. Sedimentation and structural development of big Horn basin. AAPG Bull. 49, 1867–1877.
Van der Meulen, B., Gingerich, P.D., Lourens, L.J., Meijer, N., van Broekhuizen, S., van Ginneken, S., Abels, H.A., 2020. Carbon isotope and mammal recovery from extreme greenhouse warming at the Paleocene-Eocene boundary in astronomically-calibrated fluvial strata, Bighorn Basin, Wyoming, USA. Earth Planet. Sci. Lett. 534, 116044.
Wang, C., Adriaens, R., Hong, H., Elsen, J., Vandenberghe, N., Lourens, L.J., Gingerich, P. D., Abels, H.A., 2017. Clay mineralogical constraints on weathering in response to early Eocene hyperthermal events in the Bighorn Basin, Wyoming (Western Interior, USA). Geol. Soc. Am. Bull. 129, 997–1011.
Wang, Y., Barrs, T.F., Sahoo, H., Storms, J.P., Martinius, A.W., Gingerich, P., Abels, H.A., 2022a. Sandstone body character and river planform styles of the lower Eocene Willwood Formation, Bighorn Basin, Wyoming, USA. Sedimentology 69, 1–28.
Wang, C., Hong, H., Abels, H.A., Li, Z., Cao, K., Yin, K., Song, B., Xu, Y., Ji, J., Zhang, K., 2016. Early middle Miocene tectonic uplift of the northwestern part of the Qinghai-Tibetan Plateau evidenced by geochemical and mineralogical records in the western Tarim Basin. Int. J. Earth Sci. 105, 1021–1037.
Wang, A., Jiang, Q., Lyu, G., Wang, T., Zhou, B., Wei, J., Li, Y., Gu, G., Wan, L., Liu, K., Pan, H., 2022b. Fast valley landscape response to climate change in the lower Jinsha River, Southeastern Tibetan Plateau: Field investigations and numerical modeling. Geomorphology 403, 108158.
Welch, J.L., Foreman, B., Malone, D., Craddock, J., 2022. Provenance of early Paleogene strata in the Bighorn Basin (Wyoming, USA): Implications for Laramide tectonism and basin-scale stratigraphic patterns. In: Craddock, J.P., Malone, D.H., Foreman, B. Z., Konstantinou, A. (Eds.), Tectonic Evolution of the Sevier-Laramide Hinterland, Thrust Belt, and Foreland, and Postorogenic Slab Rollback (180–20 Ma), 555. Geological Society of America Special Papers. https://doi.org/10.1130/2022.2555(09).
Westerhold, T., Röhl, U., Wilkens, R.H., Gingerich, P.D., Clyde, W.C., Wing, S.L., Bowen, G.J., Kraus, M.J., 2018. Synchronizing early Eocene deep-sea and continental records–cyclostratigraphic age models for the Bighorn Basin Coring Project drill cores. Clim. Past 14, 303–319.
White, A.F., Blum, A.E., 1995. Effects of climate on chemical_ weathering in watersheds. Geochim. Cosmochim. Acta 59, 1729–1747.
White, A.F., Brantley, S.L., 2003. The effect of time on the weathering of silicate minerals: why do weathering rates differ in the laboratory and field? Chem. Geol. 202, 479–506.
Wieczorek, R., Fantle, M.S., Kump, L.R., Ravizza, G., 2013. Geochemical evidence for volcanic activity prior to and enhanced terrestrial weathering during the Paleocene Eocene thermal Maximum. Geochim. Cosmochim. Acta 119, 391–410.
Wilson, M.J., 1999. The origin and formation of clay minerals in soils: past, present and future perspectives. Clay Miner. 34, 7–25.
Wing, S.L., Harrington, G.J., Smith, F.A., Bloch, J.I., Boyer, D.M., Freeman, K.H., 2005. Transient floral change and rapid global warming at the Paleocene-Eocene boundary. Science 310, 993–996.
Winnick, M.J., Maher, K., 2008. Relationships between CO2, thermodynamic limits on silicate weathering, and the strength of the silicate weathering feedback. Earth Planet. Sci. Lett. 485, 111–120.
Yin, K., Hong, H., Churchman, G.J., Li, R., Li, Z., Wang, C., Han, W., 2013. Hydroxy-interlayered vermiculite genesis in Jiujiang late-Pleistocene red earth sediments and significance to climate. Appl. Clay Sci. 74, 20–27.
Zachos, J., Pagani, M., Sloan, L., Thomas, E., Billups, K., 2001. Trends, rhythms, and aberrations in global climate 65 Ma to present. Science 292, 686–693.
Zachos, J.C., Röhl, U., Schellenberg, S.A., Sluijs, A., Hodell, D.A., Kelly, D.C., Thomas, E., Nicolo, M., Raffi, I., Lourens, L.J., 2005. Rapid acidification of the ocean during the Paleocene-Eocene thermal maximum. Science 308, 1611–1615.
Zachos, J.C., Schouten, S., Bohaty, S., Quattlebaum, T., Sluijs, A., Brinkhuis, H., Gibbs, S., Bralower, T., 2006. Extreme warming of mid-latitude coastal ocean during the Paleocene-Eocene thermal Maximum: Inferences from TEX86 and isotope data. Geology 34, 737–740.
Zacke, A., Voigt, S., Joachimski, M.M., Gale, A.S., Ward, D.J., Tütken, T., 2009. Surface-water freshening and high-latitude river discharge in the Eocene North Sea. J. Geol. Soc. 166, 969–980.
Zeebe, R.E., Lourens, L.J., 2019. Solar System chaos and the Paleocene-Eocene boundary age constrained by geology and astronomy. Science 365, 926–929.
Zeebe, R.E., Ridgwell, A., Zachos, J.C., 2016. Anthropogenic carbon release rate unprecedented during the past 66 million years. Nat. Geosci. 9, 325–329.
Zhang, J., Sylvester, Z., Covault, J., 2020. How do basin margins record long-term tectonic and climatic changes? Geology 48, 893–897.
Zhao, C., Wang, C., Hong, H., Algeo, T.J., Yin, K., Ji, K., Song, B., Abels, H.A., Christidis, G.E., 2021. Origin of dioctahedral smectites in lower Eocene Lulehe Formation paleosols (Qaidam Basin, China). Appl. Clay Sci. 203, 106026.
Zhao, Y., Zou, X., Gao, J., Wang, C., Li, Y., Yao, Y., Zhao, W., Xu, M., 2018. Clay mineralogy and source-to-sink transport processes of Changjiang River sediments in the estuarine and inner shelf areas of the East China Sea. J. Asian Earth Sci. 152, 91–102.